

PROCESSING MESOCARBON MICROBEADS TO HIGH-PERFORMANCE  
MATERIALS FOR FRICTION APPLICATIONS

A Dissertation

Submitted to the Graduate School  
of the University of Notre Dame  
in Partial Fulfillment of the Requirements  
for the Degree of

Doctor of Philosophy

by

Christopher William Norfolk, B.S., M.S.ChE

---

Arvind Varma, Director

---

Alexander Mukasyan, Co-Director

Graduate Program in Chemical and Biomolecular Engineering

Notre Dame, Indiana

April 2005

PROCESSING MESOCARBON MICROBEADS TO HIGH-PERFORMANCE  
MATERIALS FOR FRICTION APPLICATIONS

Abstract

by

Christopher William Norfolk

Honeywell, a leading manufacturer of friction materials for aerospace applications, manufactures brakes by densifying a carbon fiber preform using chemical vapor deposition. This has two major drawbacks, namely, the high cost of the fiber preform, and the time required to densify it via CVD. To address these issues, a novel material, mesocarbon microbeads, are investigated. This relatively inexpensive and rapidly processed material has shown good friction characteristics, but unacceptable fracture toughness. Therefore, major goals are to understand the behavior of MCMB during processing, and to investigate the most effective approach to producing high-toughness materials. Dilatometry, thermogravimetric analysis, x-ray diffraction, scanning electron microscopy, pycnometry, indentation, and compact tension were used to study sintering, graphitization, and in-situ reinforcement of MCMB-based materials.

It is shown that low temperature sintering consists of two processes: neck formation via a non-densifying liquid-phase sintering mechanism  $< 800$  K, and significant sample shrinkage due to changes of true density in the region  $800 - 1200$  K. This results in material densification without decreasing porosity. During high temperature treatment, shrinkage is again accompanied by increases in theoretical density, maintaining porosity. However, observation of pore microstructures indicate that high temperature sintering mechanisms are active, which could result in overall porosity elimination given sufficiently long sintering times.

Activation energy of  $100$  kcal/mol was determined for the graphitization of MCMB. This is less than found for many other types of carbon, and indicates the effect of preferred orientation on graphitization.

Also, it is demonstrated that exothermic reactions during in-situ reinforcement can lead to undesired swelling events. Through careful processing, these are reduced or eliminated, and additional sintering is achieved. Additionally, polymeric decomposition yields nanoscale reinforcements and enhanced sintering properties. Results show that this yields materials which are more tolerant of porosity content.

Thus it is shown that the combination of excellent compressibility, low temperature sinterability, and rapid graphitization makes MCMB an attractive precursor for manufacturing carbon-based materials. Based on this, it is recommended that  $\beta$ -resin content be optimized, methods of increasing initial sample density be investigated, and techniques of reinforcement without increasing porosity be explored.

## DEDICATION

I have had almost five years to consider this dedication, but now as I come to write it I find it more difficult than I imagined.

My time here has been very full. I have wed. I have met friends and challenges in equal share. I have lost heroes. I have learned, of course, but I cannot say I have mastered. I can say, laying aside my marriage and personal life, that this time has been the toughest I can recall. Perhaps this is perception, but today it feels accurate. Graduate school has been a lonely road for me; seldom has there been calm in the storm, aid when I was weary, or encouragement to continue fighting the good fight. Having the freedom to conduct your research often means having little or no assistance in your work; working on the unknown means continually doing that which you don't know how.

How, then, to dedicate this time, this effort, this degree, this thesis? With apologies to those in my private life, including my wife, parents, and many valuable friends, I can think of only one way.

I have climbed the mountain. This is likely the pinnacle which will define and direct my future years, for better or worse. I can only dedicate this work to the man I will inevitably become.

When you look back on this time, do not remember the tribulations; there will be greater. Do not lament the difficulties which, rightly or wrongly, earned or undeserved,

have stood in your way. It is what it is. Remember only this: with the signing of this document you have overcome. You have conquered, you have prevailed, and while you may not have overwhelmed, there is but one lesson. Persevere and triumph. There can be only one toast today: Here is to *victory*.

## CONTENTS

TABLES .....	ix
FIGURES .....	x
ACKNOWLEDGMENTS .....	xiv
CHAPTER 1 INTRODUCTION .....	1
CHAPTER 2 REVIEW OF LITERATURE .....	8
2.1 Formation of Mesocarbon Microbeads .....	8
2.2 Sintering of Mesocarbon Microbeads .....	9
2.3 Liquid Phase Sintering .....	11
2.4 Graphitization .....	12
2.5 Fracture .....	13
2.6 Toughening .....	13
2.7 Other MCMB Studies .....	15
2.8 Summary .....	17

CHAPTER 3	EXPERIMENTAL PROCEDURES .....	19
3.1	Materials .....	19
3.2	Sample Production .....	19
3.2.1	Liquid Mixing .....	19
3.2.2	Drying and Calcination .....	21
3.2.3	Dry Mixing.....	21
3.2.4	Mixing Polycarbomethylsilane (PCS) .....	22
3.2.5	Compaction .....	22
3.3	Dilatometry .....	24
3.4	High-temperature Furnace .....	25
3.5	Thermogravimetric Analysis .....	26
3.6	X-ray Diffraction .....	26
3.7	Microscopy .....	27
3.8	Pycnometry .....	28
3.9	Mechanical Properties.....	28
3.9.1	Indentation .....	28
3.9.2	Compact Tension .....	29
CHAPTER 4	INITIAL SINTERING MECHANISM OF MESOCARBON MICROBEADS .....	31
4.1	Experimental Methods .....	31
4.2	Results.....	32
4.2.1	Correlations Between Processing and Final Sintering Parameters .....	32

4.2.2	Dynamics of Sample Shrinkage.....	37
4.2.3	Dynamics of Mass Loss During Sintering.....	38
4.2.4	Microstructural Transformations .....	40
4.3	Discussion.....	42
4.3.1	Shrinkage Kinetics .....	42
4.3.2	Mass Loss Analysis.....	45
4.3.3	Microstructural Transformations .....	46
4.3.4	Overall Shrinkage Model.....	47
4.4	Densification Mechanism .....	50
4.5	Conclusion .....	51
CHAPTER 5	HIGH-TEMPERATURE SINTERING AND GRAPHITIZATION.....	53
5.1	Experimental Methods .....	53
5.1.1	Sintering.....	54
5.1.2	Graphitization .....	54
5.2	Results.....	55
5.2.1	Sintering.....	55
5.2.2	Microstructure.....	58
5.2.3	Graphitization .....	60
5.3	Discussion.....	61
5.3.1	Sintering.....	61
5.3.2	Graphitization .....	62
5.4	Conclusion .....	66



CHAPTER 6	REACTION BONDING BY IN-SITU SILICON CARBIDE AND NITRIDE FORMATION.....	67
6.1	Experimental Methods .....	67
6.2	Results.....	68
	6.2.1 Reactions in Argon .....	68
	6.2.2 Reactions in Nitrogen .....	73
	6.2.3 Polymeric Decomposition.....	76
6.3	Discussion.....	78
	6.3.1 High-Temperature Swelling in Silicon / MCMB composites.....	78
	6.3.2 Polymeric Decomposition.....	81
6.4	Conclusion .....	82
CHAPTER 7	MECHANICAL PROPERTIES OF MCMB-BASED MATERIALS.....	83
7.1	Experimental Methods .....	83
7.2	Results and Discussion .....	84
	7.2.1 Fracture Toughness.....	84
	7.2.2 Fractography .....	87
	7.2.3 Hardness.....	89
7.3	Conclusion .....	89

CHAPTER 8	CONCLUSION.....	92
8.1	Summary of Work.....	92
8.2	Suggested Areas for Future Research.....	94
REFERENCES	.....	96

## TABLES

Table 3.1	Characteristics of the mesocarbon microbeads.....	20
Table 3.2	Materials used .....	20
Table 3.3	Compaction conditions .....	22
Table 4.1	Changes of relative sample mass ( $\Delta M/M_0$ , %) and density ( $\rho_f/\rho_0$ ) for different heating rates and initial sample densities .....	36
Table 4.2	Sintering parameters for different initial sample densities .....	43
Table 7.1	Superficial Rockwell hardness results for various MCMB samples .....	90

## FIGURES

Figure 2.1	Schematic of the mesocarbon microbeads .....	9
Figure 3.1	Relationship between compaction force and relative density for pure MCMB.....	23
Figure 3.2	Effect of silicon content on green relative density.....	24
Figure 3.3	Schematic illustration of dilatometer .....	25
Figure 3.4	Schematic of disc-shaped compact tension test.....	30
Figure 4.1	Changes in relative sample mass (●) , length (▼), and diameter (▲) as functions of initial density; $\Omega=1$ K/min.....	33
Figure 4.2	Dependence of final sample density as a function of initial density: (1) $\rho_f$ , (2) $\rho_f / \rho_o$ ; $\Omega=1$ K/min .....	34
Figure 4.3	Sample pycnometric density, $\rho^{pyc}$ , as a function of temperature ...	35
Figure 4.4	Final sample relative density as a function of initial relative density; $\Omega=1$ K/min .....	35
Figure 4.5 a	Typical sample shrinkage during sintering as a function of temperature .....	37
Figure 4.5 b	Typical sample shrinkage rate during sintering $d\lambda/dT$ ; $\Omega=1$ K/min .....	38
Figure 4.6 a	Results of thermogravimetric and mass spectrometry analysis; mass loss and rate of mass loss .....	39
Figure 4.6 b	Results of thermogravimetric and mass spectrometry analysis; evolution of different gas species .....	39
Figure 4.7 a	Typical microstructure of initial MCMB compacts.....	40

Figure 4.7 b	An expanded version of the rectangle shown in Figure 4.7 a.....	41
Figure 4.7 c	Typical microstructure of sintered MCMB.....	41
Figure 4.7 d	An expanded version of Figure 4.7 c .....	42
Figure 4.8	Activation energy analysis of different shrinkage regions .....	45
Figure 4.9	Rates of mass loss and shrinkage.....	46
Figure 4.10	A schematic to illustrate the effect of increasing theoretical density on sample shrinkage .....	48
Figure 4.11	Comparison of expected and observed dilatometric results for pure MCMB. — (Curve 1): observed shrinkage rate, ----(Curve 2): expected shrinkage rate .....	50
Figure 5.1	Relationship between heat treatment temperature and relative change in mass .....	56
Figure 5.2	Relationship between heat treatment temperature and relative change in length .....	56
Figure 5.3	Evolution of pycnometric density with heat treatment temperature .....	57
Figure 5.4	Dependence of relative density on heat treatment temperature .....	58
Figure 5.5 a	Typical microstructure for a sample heat treated to 1800 K.....	59
Figure 5.5 b	Typical microstructure for a sample heat treated to 2800 K for 50 hours.....	59
Figure 5.6	Graphitization kinetics at various temperatures; ★ - 2500 K, ▲ - 2600 K, ● - 2700 K, ■ - 2800 K .....	60
Figure 5.7	Master curve showing relationship between $d_{002}$ layer spacing and effective heat treatment time; ★ - 2500 K, ▲ - 2600 K, ● - 2700 K, ◆ - 2750 K, ■ - 2800 K .....	63
Figure 5.8	Ratio of rate constants versus $T^{-1}$ .....	64

Figure 6.1	Comparison of typical dilatometric results. ---- (curves 3 and 4): pure MCMB, —(curves 1 and 2): 20 vol.% Si in MCMB; W=1 °C/min in argon .....	69
Figure 6.2	Dilatometric results with extremely low heating rate of W = °C/min in range 1100 – 1500 °C. Curve 1 represents the temperature and Curves 2 & 3 the shrinkage of composite systems of 20 and 5 % Si in MCMB, respectively .....	70
Figure 6.3 a	Typical microstructure for 20 vol% Si in MCMB heat treated W=1 °C/min in argon to 1500 °C, low magnification.....	71
Figure 6.3 b	Typical microstructures for 20 vol% Si in MCMB heat treated W=1 °C/min in argon to 1500 °C, high magnification.....	72
Figure 6.3 c	Typical microstructures for 20 vol% Si in MCMB heat treated W=1 °C/min in argon to 800 °C .....	72
Figure 6.4	Comparison of typical dilatometric results. ---- (curves 3 and 4): pure MCMB, —(curves 1 and 2): 20 vol.% Si in MCMB; W=1 °C/min in nitrogen .....	73
Figure 6.5	Dilatometric results for 20 vol% Si in MCMB processed in nitrogen .....	74
Figure 6.6	Results of TGA on 28 wt.% SiC in MCMB (Curve 1) and 28 wt.% (20 vol.%) Si in MCMB (Curve 2) processed in nitrogen. Curve 3 shows the estimated conversion of Si to Si <sub>3</sub> N <sub>4</sub> based on the uptake of nitrogen .....	75
Figure 6.7	Typical microstructure for 20 vol.% Si in MCMB heat treated W=1 °C/min to 1500 °C in nitrogen.....	76
Figure 6.8	Comparison of typical dilatometric results. ---- (curve 2 and 4): pure MCMB, —(curve 1 and 3): PCS-MCMB; W=1 °C/min in argon.....	77
Figure 6.9	Typical microstructure for PCS-MCMB .....	78
Figure 7.1	Dependence of fracture toughness on volume fraction of different reinforcement phases: ■ - pure MCMB, ▲ - W addition, ☆ - WC addition.....	85

Figure 7.2	Dependence of fracture toughness on density for several different reinforcement types and amounts: ■ - pure MCMB, ▲ - W addition, ☆ - WC addition.....	86
Figure 7.3 a	Fracture surface of pure MCMB sample .....	87
Figure 7.3 b	Fracture surface of sample with 15 vol% tungsten.....	88
Figure 7.3 c	An expanded view of the fracture surface are shown in 7.3 b.....	88

## ACKNOWLEDGMENTS

I would like to recognize here a number of people who aided me in my time as a graduate student:

- My advisors, whom I will thank in turn:
  - Dr. Varma, who I hope finds as much pride in his last Notre Dame student as he did in his others
  - Dr. McGinn, who I have appreciated for his attitude almost as much as for his extensive expertise
  - Dr. Mukasyan, for whose sake I will endeavor to stay positive
  - Dr. Hayes, who I wish I had made more time for
- Drs. Edmundo Corona and Ryan Roeder, without whom I fear I would have never achieved any measurement of mechanical properties
- Darrel Johnson, Ricky Thompson, and Ken Thompson, of Honeywell, for their invaluable assistance
- My loving wife, Noelle
- My parents and family
- My colleagues and friends, specifically Nick Martino, Robbie “Coach” Landis, Mark Kelly, Jacob Crosthwaite, Tyler and Stephanie Schmidt, Tim Marrow, Mark Black, James Cooper, Arun Ramchandran, Mike Lundin, Phil Wingert, Ryan



Gwaltney, Adrienne and Rob Minerick, Bill and Shelia Haynes, Jenn Anthony,  
David and Julie Eike, Stephen Schuyten, Ben Wilhite, Chris and Molly O'Neil,  
Kishori Deshpande, Peter Erri, and Changjun Zhou

- My mentor, Dr. Scott Husson
- The Honeywell-Notre Dame Research Alliance for funding my project
- Netzsch Instruments for performing TGA/MS free of charge

## CHAPTER 1

### INTRODUCTION

Carbon is a unique element that has an extraordinary ability to combine with itself and other elements in a variety of ways, resulting in a vast number of structural forms of solid carbon. This allows a wide range of physical properties which can be engineered for a multitude of applications.

These possibilities are enabled by the bonding structure of carbon. By promotion and hybridization,  $sp^3$ ,  $sp^2$ , and  $sp^1$  bonds are formed. In one state, four equivalent  $2sp^3$  hybrid orbitals extend tetrahedrally from the carbon atom. These form sigma bonds by overlapping with orbitals from another atom, which are easily observed in ethane,  $C_2H_6$ . Another type of bond is formed by hybridization of the valence electrons to form three  $2sp^2$  orbitals, which leaves one unhybridized 2p orbital. The three equivalent orbitals are coplanar and equidistant around the carbon atom. Atoms hybridized in this manner can form sigma bonds by overlapping  $2sp^2$  orbitals, leaving the 2p orbitals to form a second bond known as a pi bond, as seen in ethylene,  $C_2H_4$ . Predictably, a third type of hybridization results in two  $2sp^1$  orbitals and two unhybridized 2p orbitals, which results in the ability to form three bonds between two carbon atoms, as in ethyne,  $C_2H_2$  [McEnaney, 1999].

Another example of carbon's unique bonding ability is aromatic benzene,  $C_6H_6$ . This planar molecule has six carbon atoms arranged as a regular hexagon, the ideal array for creation of strain-free  $sp^2$  sigma bonds. The unhybridized 2p orbitals are used for forming pi bonds which are highly delocalized, contributing to the stability of the molecule. Polynuclear aromatic carbons consist of a number of fused benzene rings, which allow for delocalization of pi bonds through the entire molecule [McEnaney, 1999].

This polynuclear structure is very similar to the structure of graphite, which is the stable, thermodynamic equilibrium crystalline form of carbon [Fishbach, 1971]. The basis for the graphite crystallite is the graphene plane, which consists of an extended hexagonal array of carbon atoms with  $sp^2$  sigma bonds and delocalized pi bonds. The length of the bonds between carbon atoms within the graphene plane is 142 pm, which is between the length of  $sp^3$  and  $sp^2$  bonds, 153 and 132 pm, respectively. The resonance structures show that each carbon-carbon bond possesses about one third double bond character. These planes are stacked to form the three-dimensional graphite structure [McEnaney, 1999].

The size and perfection of these planes are important in application of many carbons and graphites. The distance between carbon planes, 335 pm, is much larger than the distance between carbon atoms in the same plane, 142 pm. This suggests that contribution of pi bond overlap to interlayer bonding is negligible. It has commonly been assumed that interlayer bonding is dominated by van der Waals forces, which are much weaker than the chemical bonds observed within graphene planes. There are two orders possible for stacking graphene planes; rhombohedral, which has a stacking sequence

ABCABC, and hexagonal, the more stable form, with the stacking sequence ABAB [McEnaney, 1999].

While there are several types of carbon materials, including diamond, carbon nanotubes, and Fullerenes, the vast majority of engineering carbons have either a graphitic or disordered graphitic microstructure. There are two major properties that make the graphite structure so applicable. The first is its ability to withstand exceptionally high temperatures, up to 4450 K, without melting, which makes it the material of choice for such conditions. The second involves the structure of graphite discussed above. Aromatics produce high Young's modulus and tensile strength, as well as high thermal and electrical conductivity within the plane. However, weak bonding between the layers results in the same properties being low when measured between the planes. Materials with properties dependant on the direction of the measurement, are said to have a large amount of anisotropy [McEnaney, 1999].

The drive to increase the mechanical properties of materials used for military aircraft shortly after World War II led to the advent of carbon fiber technology. Boron fibers were initially used to reinforce plastics, but this proved unsuitable due to the fiber costs. Glass fibers have also been used, and improved quality glass has allowed wide spread use of these low-cost, relatively high-strength fibers. However, the strength and stiffness of carbon fibers is superior to that of all other reinforcing fibers. These advanced properties are due to the anisotropic graphite crystal. Great care is taken during the processing of carbon fibers to ensure that the graphene planes are arranged parallel to the fiber axis, allowing the mechanical properties to be dominated by aromatic bonding within graphite layers [Fitzer and Manocha, 1998].

The first appearance of carbon / carbon composites was in the space program in the 1960s. Thermal protection for the space shuttle required a lightweight, high temperature resistant material, that maintained strength at high temperatures, and had high resistance to thermal shock. Graphite, with its anisotropic properties, could fulfill most of these requirements, but the mechanical properties of most engineering carbons had not approached the theoretical limit and therefore required strengthening. Composite fabrication techniques developed in the era gave impetus to carbon / carbon composites. This spawned an intense period of research that ushered in improvements to both carbon fiber and matrix precursors and development of weaving techniques. Since then, carbon / carbon materials have found use in a variety of applications, including tools for the glass industry, heating elements for furnaces, crucibles, and friction materials [Fitzer and Manocha, 1998]. Carbon materials are ideally suited for use in wear related applications, e.g., brakes for vehicles such as automobiles and aircrafts. It is known that shoe leather was the material first used for aircraft brakes, as in the Wright brothers' first flights. Carbon-based materials have many advantages over shoe leather. Because the frictional torque accompanying deceleration of a vehicle results in heat generation on the order of several hundred mega joules, the brake is required to absorb and dissipate energy without compromising its structural integrity. Therefore, resistance to high temperatures, high thermal conductivity, and high heat capacity are of primary interest, and excellent friction and wear characteristics add to their advantageous implementation. Carbon fibers have good friction and wear characteristics along their length, and thus early carbon / carbon brake materials were designed with fibers arrayed parallel to the braking surface. However, since the friction performance of the system is strongly dependant on

temperature, it is also desirable to conduct heat from the friction surface into the bulk of the material at high rate. This requirement, coupled with other structural, mechanical, and frictional requirements, led to the development of several different fiber orientations within the brake disk which meet the strict needs of the application [Fitzer and Manocha, 1998].

Another advantage of using carbon materials in friction applications involves their wear mechanism. As manufactured, the surface has a large number of asperities, which limit the contact surface area available for breaking. However, as the ridges are forced to slide past each other by the large braking energy, they are sheared away from the surface. This increases the surface area and grinds the carbon into a “friction film” that protects the wear surface by acting as a solid lubricant, lowering the coefficient of friction and reducing the wear rate [Fitzer and Manocha, 1998].

Honeywell is a leading producer of friction materials for aircraft applications. One manufacturing process involves densifying a carbon fiber preform using chemical vapor deposition (CVD). There are two major drawbacks to this approach. The first is the high cost of the carbon fiber preform, which represents up to 50% of the total manufacturing cost. The second is the time needed to fully densify the preform via CVD, which is performed in repetitive cycles that require at least 130 days to complete. Clearly, profits can be increased by decreasing manufacturing costs, and so advancements which address either of these issues are desired.

There are several directions by which this problem can be addressed. The cost efficiency of the carbon fiber can be increased, either by increasing mechanical properties (thereby reducing the amount of fiber required) or by reducing fiber costs. There have

also been studies on increasing the efficiency of CVD by modifying the process. Further, by optimizing the choice of materials and processes, other improvements may be realized.

The drive toward innovation in both materials and processes used to manufacture friction materials led engineers at Honeywell to begin experimentation with mesocarbon microbeads (MCMB). This material is derived from pitch and has been recognized as an excellent precursor to parts with high density and strength. The ability of MCMB to self-sinter at relatively low temperatures has attracted considerable attention in the literature [Ozaki and Nishiyama, 1987; Bhatia et al., 1997; Wang et al., 1999a; Wang et al., 1999b; Wang et al., 1999c; Aggarwal et al., 2000]. Honeywell discovered that the friction and wear characteristics of MCMB-derived materials were good, however, their fracture toughness was unacceptably low [Dillon et al., 1998]. Accordingly, the major goals for this thesis are (a) to understand the behavior of mesocarbon microbeads during processing (sintering, graphitization, etc.) to learn how to best tailor the material properties, and (b) to investigate the most effective processing procedure to produce high-toughness material for use in friction applications.

This thesis is divided into several Chapters. In Chapter 2, a review of the available literature pertaining to MCMB is provided, and the major goals for this work are formulated. The experimental procedures used are described in Chapter 3.

As mentioned previously, MCMB have a unique ability, among carbon materials, to sinter at relatively low temperatures. Although sintering in MCMB has been described, a systematic study is lacking. Chapter 4, therefore, is a detailed study of the

sintering mechanism. Based upon the obtained results, recommendations to manufacture high density and strength materials are made.

Chapter 5 is a continued exploration of the sintering mechanism of MCMB, undertaken at high temperatures. Concurrently, this chapter describes the kinetics of graphitization in MCMB, and discusses it in the context of other carbon materials. Chapters 4 and 5 represent efforts made to understand the material and learn how to process MCMB materials most effectively.

One common approach to improve the fracture toughness of brittle materials is to introduce reinforcement in the form of particulates. Chapter 6 details efforts to form reinforcement particulates in-situ, by reactions with silicon to form silicon carbide and nitride. Using this route, the sintering ability of the carbon may be enhanced via reaction bonding mechanisms. Chapter 7 discusses the mechanical properties of MCMB-based materials. Finally, some conclusions of the present work, and suggestions for future research, are summarized in Chapter 8.



## CHAPTER 2

### REVIEW OF PRIOR LITERATURE

As noted in Chapter 1, mesocarbon microbeads (MCMB) represent an emerging approach to the formation of carbon materials for use in advanced technological applications. This chapter examines, in detail, the published research concerning the use of MCMB.

#### **2.1    *Formation of Mesocarbon Microbeads***

It has long been known that when pitch is heat treated, a mesophase appears [Brooks and Taylor, 1965]. Pitch is a mixture of polynuclear hydrocarbons with an average molecular weight of  $\sim 200$  AMU. Upon heating to approximately  $200\text{ }^{\circ}\text{C}$ , it becomes fluid. In the melt, the translational energy afforded to molecules by the temperature exceeds the cohesion energy. However, elevated temperature initiates dehydrogenation polymerization reactions, causing average molecular weight to increase, and this reaches  $600 - 900$  AMU when the temperature is  $> 400\text{ }^{\circ}\text{C}$ . As the molecules grow, the cohesive energy exceeds the translational energy, resulting in the homogeneous nucleation of a new phase, called the mesophase [Marsh and Menendez, 1989].

The polyaromatic molecules that constitute pitch are discotic, as alluded to in Chapter 1, with one axis much smaller than the other two. These molecules arrange themselves with the planes parallel to each other, forming nematic liquid crystals [Collings and Hird, 1997]. The growing liquid crystal phase adopts a spherical shape to minimize surface energy [Marsh and Menendez, 1989]. Thus, the mesophase creates microbeads, which have diameters up to 100  $\mu\text{m}$  [Moriyama et al., 2000]. A schematic of the microbeads is shown in Figure 2.1.

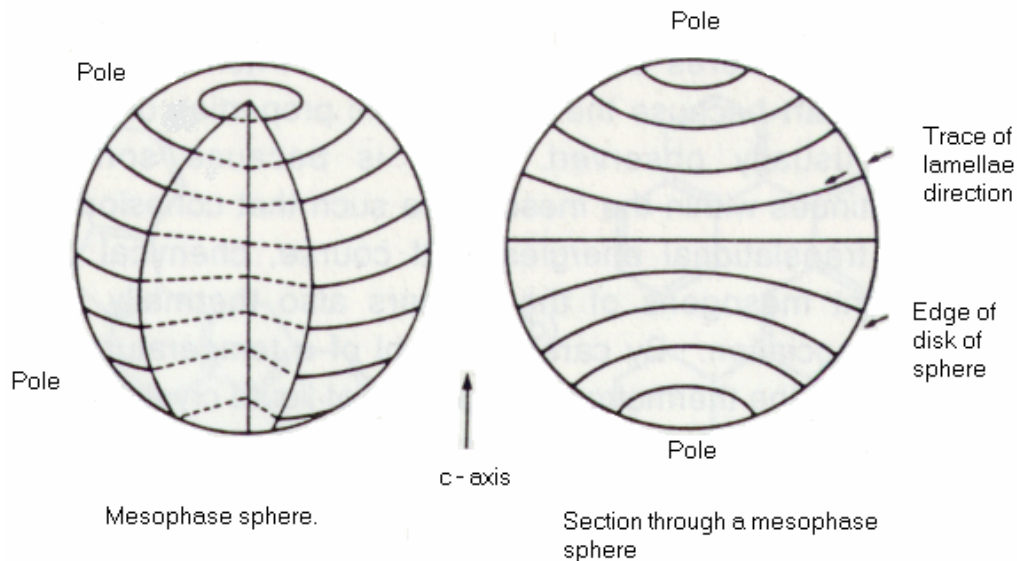


Figure 2.1: Schematic of the mesocarbon microbeads

## 2.2 *Sintering of Mesocarbon Microbeads*

As stated in Chapter 1, the ability of MCMB to self-sinter has been studied previously. It has been widely observed that MCMB undergoes sintering at a relatively low temperature. Studies of this phenomenon are detailed next.

Nagayama et al. [1993] of the Kawasaki Corporation made the first known study of the sintering of MCMB, or Kawasaki mesophase fine carbon (KMFC) as they

described it. The focus of this report was the sintering mechanism of KMFC. It was concluded that sintering in the liquid phase proceeds through fusion of the  $\beta$ -resin between 400 and 600 °C. The  $\beta$ -resin is a particular weight fraction of the parent pitch material, defined as the fraction soluble in quinoline but insoluble in benzene, that remains on the surface of the MCMB when extracted. Further, it was claimed that the liquid phase sintering promotes adhesion between particles by removing macropores at the interface, and that solid phase sintering decreases porosity at higher temperatures. Although this study was limited to temperatures less than 1000 °C, relatively high levels of sample shrinkage (~12 %) were observed.

Although not explicitly studying MCMB, Martinez-Escandell et al. (1999) drew pertinent conclusions by studying the effect of multiple extraction / washing steps on the sinterability of mesophase powders. It was deduced that washing changes the behavior of the  $\beta$ -resin, which controls the sintering behavior. Similar conclusions were made by Aggarwal et al. [2000], who observed that calcinations also influence the behavior of the  $\beta$ -resin and, thereby, the sintering process.

A major study specifically carried out on MCMB sintering was undertaken by Gao et al. [2003]. Observations of changes in mass, dimensions, density and conductivity led to the conclusion that viscous sintering occurs below 600 °C and that solid carbonization causes the shrinkage observed above 600 °C. Again, relatively high levels of shrinkage were observed. Cavities located at the interface between MCMB grains were claimed to gradually disappear during plastic sintering.

### 2.3 *Liquid Phase Sintering*

The studies of both Gao and Nagayama claim that viscous or liquid phase sintering occurs at temperatures below 600 °C. Thus, some background on liquid phase sintering is useful.

Classic liquid phase sintering consists of three stages. Upon formation of a liquid phase, capillary forces are exerted on the solid particles, resulting in rearrangement. This can cause rapid densification or swelling, depending on the characteristics of liquid – solid interaction. As rearrangement slows, a stage of solution and reprecipitation begins. In this stage, solubility and diffusivity effects become dominant. Liquid phase sintering represents a major advantage over conventional solid state sintering because diffusion through the liquid phase is much faster than through a solid phase. Material from small solid grains is dissolved in the liquid phase and is transported to large grains, causing pores to shrink and grains to grow. The last stage is solid state sintering. Further densification can be obtained by sintering between solid particles in contact, but the process is slow [German, 1985].

Liquid phase sintering, as applied to a related system known as mesophase powders, was studied extensively by Hoffmann and Hüttinger [1993, 1994]. They described the viscosity behavior as decreasing through temperature increases until it increased due to chemical reactions in the mesophase [Hoffman and Hüttinger, 1993]. Further, it was shown that the volume shrinkage caused by liquid phase sintering is quite small. The majority of shrinkage was attributed to solid-phase sintering [Hoffman and Hüttinger, 1994]. The mesophase powders described result from heat treatment of pitch after MCMB are formed. This yields a material with large mesophase content resulting

from coalescence of microbeads. While fundamentally different, this example is useful in understanding the behavior of the  $\beta$ -resin during sintering of MCMB.

## **2.4    *Graphitization***

It is well known that graphite is the stable, thermodynamic equilibrium structure of carbon [Fischbach, 1971]. However, carbon exists metastably in other crystallographic forms also, such as that found in MCMB. Upon heating, the “mesophase” structure of MCMB undergoes crystallographic transformations to the more ordered structure of graphite. Much effort has been placed in studying the kinetics of this change. The rate of graphitization of carbon materials increases with increasing heat-treatment temperature, pressure or applied stress. This indicates that graphitization is a thermally activated process. Also, it is not possible to represent graphitization kinetics by any simple law [Pacault, 1971]. Further, it has been shown that isothermal graphitization data may be superimposed by translations along the time axis, which requires the activation energy to be constant with temperature. Some researchers have concluded that this activation energy is indicative of the basic mechanism by which graphitization occurs, which applies universally to all graphitizing carbons. However, the effect of preferred orientation, while generally agreed to be important in determining graphitizability, remains largely unknown and may be complex [Fischbach, 1971].

## **2.5     *Fracture***

The fracture behavior of graphite is not easily understood. It is pseudo-brittle, with a limited degree of plasticity. However, the dominant factor is known to be the flaw structure within the graphite. A flaw under the influence of local stresses results in formation of a macroscopic crack that extends to cause failure. The failure mechanics can be understood through the fracture mechanisms developed for other brittle materials such as ceramics [Romanoski and Burchell, 1999].

In ceramics, porosity is deleterious to fracture toughness. Pores remaining in graphitized samples will decrease mechanical properties by two mechanisms. First, pores reduce the area across which load is applied. Second, pores act as stress concentrators [Callister, 1997]. Therefore, the total porosity of samples after graphitization must be as low as possible to give high toughness parts.

## **2.6     *Toughening***

Ceramics are commonly toughened by the addition of reinforcement phases. The mechanisms of toughening are discussed here.

Modulus transfer generally involves high elastic modulus fibers reinforcing a lower elastic modulus matrix. The stress applied to the composite is “transferred” from the matrix to the fibers due to their higher modulus and cohesive strength. This toughening mechanism primarily involves continuous fibers as reinforcement.

Since ceramics generally fracture in tension, prestressing can increase a sample’s resistance to crack propagation. For this, a portion of the ceramic is placed under a

residual compressive stress. Thus, a crack cannot propagate through this section, and fracture will occur only after the prestress energy has been overcome.

A toughening mechanism that is present in almost every ceramic, to some extent, is crack deflection or impediment. The fracture toughness of a ceramic is strongly influenced by the microstructure and path that the crack follows through the material. If the crack path is planar and smooth, the new surface area created is minimized, and the fracture energy required is low. However, if the crack is deflected, then the surface area created increases, and thus the fracture energy required increases. Crack deflection can be accomplished by grain boundaries in polycrystalline ceramics and also by elongated or fibrous grain structures, dispersions of foreign particles, plates, whiskers, or chopped fibers.

Crack bridging is another toughening mechanism. This involves a microstructural feature that extends across the propagating crack and imposes a closing force on it. Inhibiting crack opening reduces the stress intensity at the tip, slowing expansion. This mechanism is also observed primarily for fiber or whisker reinforced ceramics, but there has been evidence of bridging for fibrous microstructures and platelet shaped reinforcements.

Pullout is a toughening mechanism that often accompanies crack bridging. If a fiber, particle, or grain debonds from the adjacent microstructure and is pulled out as the crack opens, energy is dissipated in the form of friction between the reinforcement and the matrix, reducing the energy available for propagation.

Finally, the stress at the crack tip is reduced by a stress-induced microstructural change, known as crack shielding. The change occurs around the crack tip and extends

along the propagating crack. Microcracking and transformation toughening both result in crack shielding [Richerson, 1992].

## **2.7 Other MCMB Studies**

There has been much work using MCMB for various applications. One of the most studied is the use of MCMB-based materials for anodes in lithium ion batteries. This application is outside the scope of the present work and will not be discussed. Research focused on heat treatment of the MCMB, the formation of structural members, and the processing of composites are described here.

Studies involving the modification of MCMB formation by the addition of carbon black (CB) to the parent pitch have been the focus of Wang et al. [1999]. This is a logical extension of the known effect of CB on mesophase pitch, namely, suppressing the expansion of the mesophase during carbonization by hindering growth of molecular stacking, increasing the viscosity of the pitch matrix, and providing a pathway for evolved gases to escape (along the surface of the CB particles). It is shown that CB promoted dehydrogenation reactions during MCMB formation (see section 2.1), led to higher molecular weight and increased carbon yield [Wang et al., 1999b]. While CB disrupts the ability of MCMB to graphitize, it also inhibits crack propagation [Wang et al., 1999c].

Hu et al. [2003, 2004] also studied MCMB, by making carbonaceous laminations using tape casting of MCMB-based slurries. For this they added a water-soluble binder, which is interesting because it is generally believed that  $\beta$ -resin acts as a binder, eliminating the need for such additives. They optimized the amount of binder,



plasticizer, and dispersant so as to maintain a stable slurry of suitable viscosity for processing [Hu et al., 2003]. The effect on graphitization of several dopants was also reported, including Ti,  $\text{ZrO}_2$ , and  $\text{B}_4\text{C}$ . It was concluded that Ti, which reacts during processing to form TiC, is most effective, showing the largest increases in bending strength [Hu et al., 2004].

A study of the tribological performance of MCMB was reported by Xiaohao et al. [2003]. For this, MCMB heat-treated to different degrees were mixed with liquid lubricants and the mixture tested for its lubrication properties. It was observed that the frictional properties depend on the structure of MCMB, which is controlled by the degree of heat treatment. It was further observed that testing, which includes the movement of surfaces past each other under pressure, induces structural rearrangement resulting in increased graphitization.

Similar to that observed by Wang et al., Mirhabibi et al. [2003] report that graphite flake carbon serves as an effective reinforcement phase, increasing the work of fracture. This is due to crack deflection, crack bridging, and pullout.

Gao et al. [2002] prepared a carbon – carbon composite using MCMB as matrix and chopped fibers as reinforcement. It was observed that the properties of the composite are increased by carefully controlling the oxidation of fibers, which determines the fiber – carbon interfacial adhesion.

It is clear that research is progressing in several directions. As suggested in section 2.6, much work is ongoing in using reinforcements to toughen MCMB-based materials, and some success has been achieved. Additionally, evidence given by Hu et al.

has shown that in situ reinforcement formation (as observed when using Ti as a dopant) can be effective in increasing mechanical properties.

## **2.8    *Summary***

As noted above, prior studies on sintering of MCMB have observed high levels of shrinkage during sintering. It was concluded that the pore content should decrease via liquid phase sintering. In normal sintering systems, these two properties, shrinkage and porosity, are easily related. However, their relationship is complicated in carbon materials owing to changing density. It is well known that the density of many carbon materials evolves during heat treatment [McEnaney, 1999]. Therefore, it is unclear if shrinkage indicates reduction of porosity or increasing density. This relationship must be determined, as pore content is an important parameter that must be strictly controlled, as discussed in section 2.5. This relationship, in the overall context of the sintering mechanism, is explored in Chapter 4, and the consequences discussed.

As MCMB is a special carbon with extraordinary sintering characteristics at relatively low temperatures, there may also be unique high temperature sintering mechanisms. These would occur in concert with graphitization. The physical properties of MCMB-based materials may be related to the state of graphitization, as they are in many carbon fiber systems [Fitzer and Manocha, 1998]. Additionally, questions concerning the kinetics and mechanism of graphitization persist. Chapter 5 discusses observations concerning high-temperature sintering and kinetics of graphitization in MCMB.

Investigating the most effective processing procedures to produce high-toughness materials is a stated goal of this work. As discussed in section 2.6, several toughening mechanism can be used. Studies involving the processing of composite systems, with in-situ formation of reinforcement particulates, are reported in Chapter 6.

The evaluation of the mechanical properties of MCMB-based materials is reported in Chapter 7.

## CHAPTER 3

### EXPERIMENTAL PROCEDURES

The techniques, equipment, and procedures used in preparing, processing, and testing MCMB-based materials are described in this chapter.

#### **3.1    *Materials***

This section gives the details of all materials used in this work. The MCMB was obtained (Osaka Gas, Japan, 6G) free of charge. Its characteristics are summarized in Table 3.1. The suppliers, stock numbers, and important properties of all other materials used are given in Table 3.2.

#### **3.2    *Sample Production***

All procedures involved in preparing the green parts are described in this section.

##### **3.2.1   *Liquid Mixing***

A liquid mixing procedure was used to introduce reinforcement particulates to the MCMB in some cases, as discussed in Chapter 6.

TABLE 3.1

## CHARACTERISTICS OF THE MESOCARBON MICROBEADS

<b>Particle Size</b>	10 % < 0.66 $\mu\text{m}$ 50 % < 5.34 $\mu\text{m}$ 90 % < 14.22 $\mu\text{m}$
<b>Toluene Insoluble Content</b>	95.6 wt %
<b>Quinoline Insoluble Content</b>	91.2 wt %
<b><math>\beta</math>-Resin Content</b>	4.4 wt %

TABLE 3.2

## MATERIALS USED

<b>Material</b>	<b>Supplier and Location</b>	<b>Stock Number</b>	<b>Important Property</b>
Silicon, Si	Elkem, Norway	----	Average particle size < 2 $\mu\text{m}$
Silicon Carbide, SiC	Nanostructured and Amorphous Materials, New Mexico	4610HT	Average particle size 130 nm
Polycarbomethylsilane, PCS	Aldrich, Missouri	52258-9	Melting point 79 $^{\circ}\text{C}$
Tungsten, W	Alfa Aesar, Massachusetts	44210	Average particle size < 1 $\mu\text{m}$
Tungsten Carbide, WC	Alfa Aesar, Massachusetts	12482	Average particle size < 1 $\mu\text{m}$
Titanium, Ti	Alfa Aesar, Massachusetts	10383	100 mesh
Titanium Carbide, TiC	Nanostructured and Amorphous Materials, New Mexico	----	Average particle size 130 nm
Titanium Nitride, TiN	Alfa Aesar, Massachusetts	41556	325 mesh
Ethanol	Aaper Alcohol, Kentucky	----	200 proof

The powders were measured in the desired ratio and wet-mixed in ethanol by ultrasonic bath (Branson 2200) for at least two hours. The ethanol was driven off via hot plate (Corning PC-351) under moderate stirring. The product was treated in a high-energy ball mill (Spex 8000) to reduce agglomeration. The material was collected and dried using the procedure described in section 3.2.2.

### **3.2.2 *Drying and Calcination***

All materials used were subjected to the following procedure prior to compaction. The material was placed in a furnace (Precision Economy Oven) maintained at 100 °C for 12 hours in air. This procedure serves several purposes: (1) to remove residual ethanol from systems which were liquid mixed according to the procedure described in 3.2.1; (2) to remove water which may be absorbed on the surface of the powder; (3) to cause a mild oxidation of the MCMB which was qualitatively observed to improve final sample quality [Wang et al., 1999c; Aggrawal et al., 2000].

### **3.2.3 *Dry Mixing***

A dry mixing procedure was used to introduce reinforcement particulates to the MCMB in some cases, as described in Chapter 7. Calcined MCMB (see section 3.2.2) and reinforcement powders were measured in the desired ratio and high-energy ball milled (Spex 8000) for 15 minutes.

### **3.2.4 Mixing Polycarbomethylsilane (PCS)**

A Si-containing polymer,  $(C_2H_6Si)_n$ , was used to produce reinforcements in MCMB, as noted in Chapter 6. The mixing procedure for this system involved first dispersing PCS in ethanol on a hot plate (Corning PC-351) under vigorous stirring. Calcined MCMB (see section 3.2.2) was added to the solution and the ethanol driven off. The material was collected and ball milled to reduce agglomeration (Spex 8000).

### **3.2.5 Compaction**

Green samples were uniaxially compacted (Carver Autoseris) using dies of different sizes. Table 3.3 summarizes the conditions used.

TABLE 3.3

COMPACTION CONDITIONS

<b>Die Size</b>	<b>Pressure</b>	<b>Duration</b>	<b>Chapter</b>
10 mm	50 – 300 MPa	3 minutes	Chapter 4
31 mm	60 MPa	9 minutes	Chapter 5
5 mm	400 MPa	3 minutes	Chapter 6
31 mm	300 MPa	9 minutes	Chapter 7

The applied load is directly related to the sample green density achieved. The relationship between compaction pressure and green relative density for pure MCMB is shown in Figure 3.1. The addition of reinforcement particulates affects the compressibility of the composite. In general, under a constant pressure, increasing the volume fraction of reinforcement decreases the green relative sample density, as illustrated by the MCMB-Si system shown in Figure 3.2.

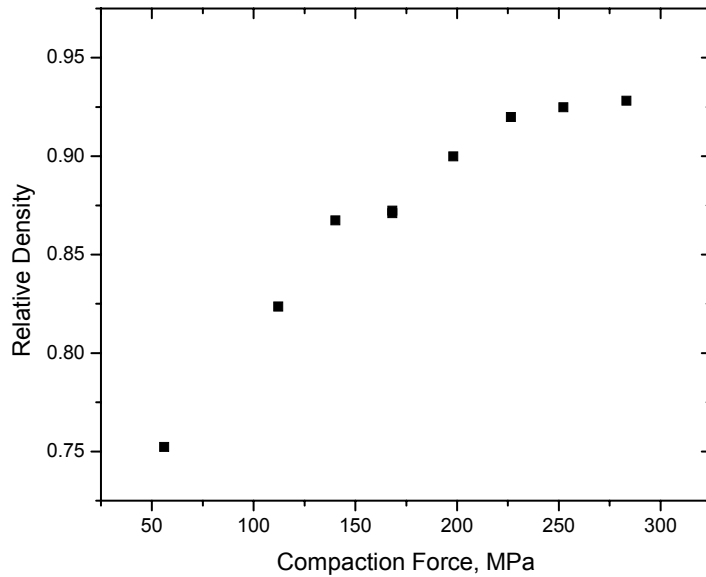


Figure 3.1: Relationship between compaction force and relative density for pure MCMB



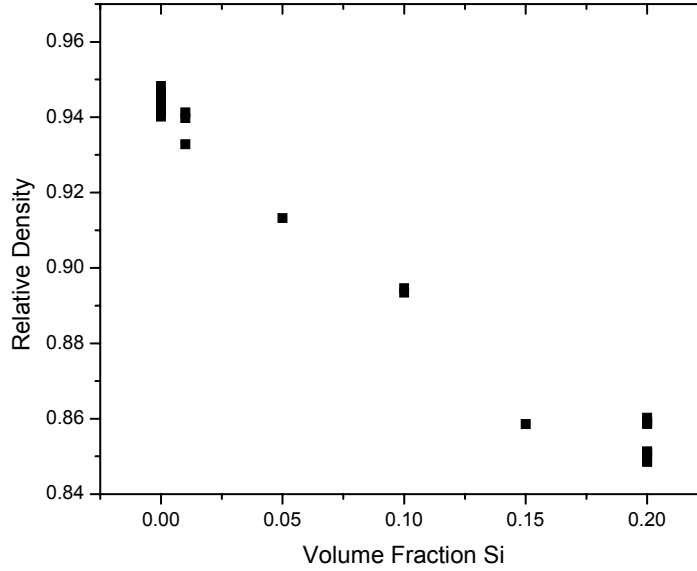


Figure 3.2: Effect of silicon content on green relative density; compaction pressure 400 MPa

### 3.3 *Dilatometry*

Compacted green samples were studied using dilatometry. This experimental technique allows the change in a sample's length to be monitored during heat treatment (see Figure 3.3). The sample is held by a sample holder and is contacted by a push-rod. The other end is outside the hot zone, and has a small metal core attached to it, positioned inside a linear variable differential transformer (LVDT) that produces a differential voltage output which varies linearly with changes in the core position. The dilatometer is calibrated to account for thermal expansion of the sample holder and push rod, using either a single crystal sapphire or polycrystalline alumina.

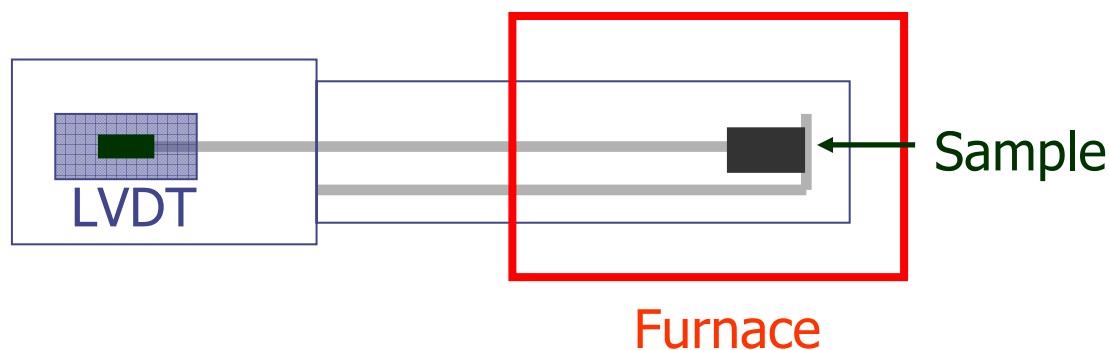


Figure 3.3: Schematic illustration of dilatometer

Two dilatometers were employed in this work. The first dilatometer (Harrop TDA-H1-PP6) was used to collect all data reported in Chapter 4. This horizontal dilatometer operated with a flowing nitrogen atmosphere and was calibrated using a single crystal sapphire (Anter Corp). The second dilatometer (Linseis L75HD1550) was used to collect all data reported in Chapter 6. This horizontal dual push-rod dilatometer was used with a flowing atmosphere of either nitrogen or argon and calibrated with polycrystalline alumina (Linseis); the unit was capable of accuracy to 10 nm, temperatures to 1500 °C, and heating rates of 30 °C/min.

### 3.4 *High-temperature Furnace*

A graphite resistance furnace was used for heat treatment of green compacts (as in Chapter 7) and also of MCMB as loose powder (Chapter 5). This furnace (Astro 1000-2560-FP20) has a water cooling jacket, a hot zone 2 inches in diameter and 6 inches in height, and is capable of reaching 2900 °C and sustaining temperatures of up to 2700 °C. The furnace was retrofitted with a controller (Eurotherm 2416), optical pyrometer (Raytek Thermalert 3 Plus), and C-type thermocouple with tungsten sheath and

thermocouple retractor (Thermal Technologies). Temperature control was accomplished by thermocouple below 1000 °C, and by pyrometer at higher temperatures. The pyrometer was calibrated over the range 1300 – 2300 K by the thermocouple and by the melting of niobium foil at 2741 K. The furnace was operated with a pressurized helium atmosphere that was 5 – 10 psi higher than atmospheric value.

### **3.5 *Thermogravimetric Analysis***

Thermogravimetric analysis was performed using two instruments. The first (Netzsch STA 449 C Jupiter) was connected to a mass spectrometer (Netzsch MS 403 C Aeolos). This combination allowed for thermal analysis of the sample and identification of evolved gases. The unit was operated at 5 °C/min with a flowing argon atmosphere. Netzsch conducted these experiments free of charge. The obtained results are presented in Chapter 4. The second instrument (TA Instruments SDT 2960) was used to study the reaction of silicon to silicon nitride during reaction bonding of MCMB-Si systems. This was done with a 10 °C/min heating rate and a flowing nitrogen atmosphere to temperatures < 1500 °C. These results are presented in Chapter 6.

### **3.6 *X-ray Diffraction***

X-ray diffraction (XRD) (Scintag X1 advanced diffractometer) was used to monitor composition, reaction progression, and graphitization. The results are discussed in Chapters 5, 6, and 7. Powder XRD was performed, and when required, samples were crushed using a mortar and pestle. For detailed measurements required to study

graphitization (Chapter 5), silicon was added as an internal standard [Iwashita et al., 2004].

The  $2\theta$  value where the carbon peak was observed was corrected according to the position of the silicon peak using the equation

$$2\Theta_C^{true} = 2\Theta_C^{obs} + \left[ 2\Theta_{Si}^{true} - 2\Theta_{Si}^{obs} \right] \quad (3.1)$$

where  $2\Theta_C^{obs}$  and  $2\Theta_{Si}^{obs}$  are the observed values of carbon and Si peaks, respectively,  $2\Theta_C^{true}$  is the corrected position of the peak, and  $2\Theta_{Si}^{true}$  is the true position of the Si peak. Studies of the  $d_{002}$  peak of carbon were conducted, using XRD scans of the range  $2\theta=[21, 30]$ . The carbon peak was generally observed around  $2\theta \sim 26^\circ$ , and  $2\Theta_{Si}^{true} = 28.4429^\circ$ . The layer spacing was then calculated from

$$d_{002} = \frac{\lambda}{2 * \sin\left(\Theta_C^{true} * \frac{\pi}{180}\right)} \quad (3.2)$$

where  $d_{002}$  is the layer spacing in Angstroms,  $\lambda$  is the wavelength of the x-rays used (1.540562 Å), and the term  $\pi/180$  is used to convert the value of  $\Theta_C^{true}$  from degrees to radians.

### 3.7 Microscopy

Sample microstructures were investigated utilizing two different scanning electron microscopes. The first (JEOL JSM-6300V) is located at Honeywell's facility in South Bend, Indiana. The results presented in Chapters 4 and 5 were obtained using this microscope. The second (Leo EVO 50) is located at the University of Notre Dame in the Environmental Molecular Science Institute. The microstructures shown in Chapters 6

and 7 were studied using this microscope. In general, the samples were mounted in epoxy and polished to a mirror surface prior to examination. The surface was coated with a thin layer of gold via sputtering to avoid charging of the sample. The exception to this is the fracture surface results presented in Chapter 7. These samples were not mounted, polished, or coated prior to examination, so that the details of the fracture surface would not be destroyed.

### **3.8 *Pycnometry***

In this work, the theoretical density was measured by helium pycnometry (QuantaChrome Ultrapycnometer 1000 UPY-2). When required, samples were crushed thoroughly after heat treatment, thereby opening any void space and allowing the intrinsic material density to be measured, as described in ASTM standard B923-02.

### **3.9 *Mechanical Properties***

The procedures used to measure the mechanical properties of MCMB-based materials are described in this section. The results appear in Chapter 7.

#### **3.9.1 *Indentation***

Hardness measurements were made using a Rockwell superficial hardness tester (Leco RT-370). The major load used was either 15 or 30 kg. This instrument is located at Honeywell's facility in South Bend, Indiana.

### 3.9.2 Compact Tension

Disc-shaped compact tension measurements were made to determine the fracture toughness of MCMB-based materials. These were done using ASTM E1820-01 as a guideline (see Figure 3.4). The samples were machined using electron discharge machining (EDM). They were fractured in tension (ATS 900) with a crosshead speed of 0.005 inch/min. The extension of the sample during testing was monitored using an extensometer (MTS 632.12E-20).

The load at which fracture occurs is measured and used to calculate fracture toughness according to

$$K = \frac{P}{(B^2W)^{1/2}} f\left(\frac{a}{W}\right) \quad (3.1)$$

where K is the fracture toughness, P is the load at fracture, B is the sample thickness, a and W are the dimensions indicated in Figure 3.4, and f is given by

$$f\left(\frac{a}{W}\right) = \frac{\left[ \left(2 + \frac{a}{W}\right) \left( 0.76 + 4.8\left(\frac{a}{W}\right) - 11.58\left(\frac{a}{W}\right)^2 + \frac{11.43\left(\frac{a}{W}\right)^3 - 4.08\left(\frac{a}{W}\right)^4}{\left(1 - \frac{a}{W}\right)^{3/2}} \right) \right]}{\left(1 - \frac{a}{W}\right)^{3/2}} \quad (3.2)$$

It should be noted that ASTM E1820-01, which was designed for use with metallic materials, assumes the presence of a preexisting, sharp fatigue crack at the crack initiation notch. Thus, fatigue was attempted in the hope of initiating such a crack. However, these efforts were not successful, as no cracking could be observed via SEM. Therefore, further tests were performed without special efforts to initiate cracking.

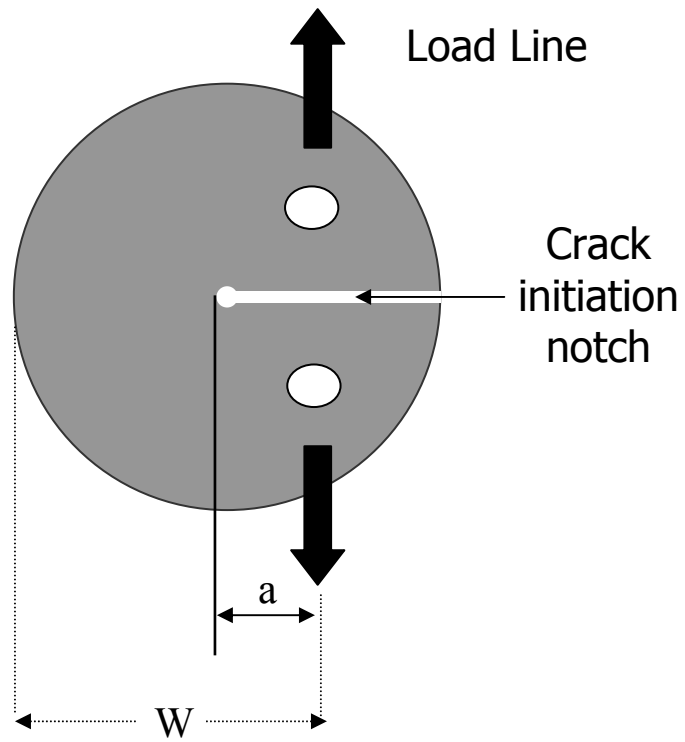


Figure 3.4: Schematic of disc-shaped compact tension test

## CHAPTER 4

### INITIAL SINTERING MECHANISM OF MESOCARBON MICROBEADS

As outlined in Chapters 1 and 2, an emerging approach to the formation of advanced carbon materials exploits the unique properties of mesocarbon microbeads (MCMB). However, relatively few prior works attempt to explain the unique self-sinterability of the MCMB [Nagayama et al., 1993; Gao et al., 2003], and analysis shows that the sintering mechanism of MCMB is not yet elucidated conclusively. Additionally, existing studies have not fully taken into account the consequences of density changes in carbon materials. In this chapter, the low-temperature sintering mechanism of MCMB is investigated. Recommendations for the development of high-toughness parts based on MCMB are made based on the results.

#### **4.1    *Experimental Methods***

It is known that the properties of polyaromatic mesophases depend on the manufacturing, extraction, and pretreatment procedures, but all of them possess the ability to self-sinter at relatively low temperatures. One type of commercially available mesocarbon microbeads (Osaka Gas, Japan) is investigated, whose characteristics are summarized in Table 3.1. The MCMB were uniaxially pressed in a 1 cm cylindrical die



to different initial densities,  $\rho_o$ , in the range 1.15-1.38 g/cm<sup>3</sup>, as described in Chapter 3. The relative sample density,  $\rho^r = (M/V)/\rho^{th}$ , was also calculated, where M is the sample mass, V the geometric sample volume, and  $\rho^{th}$  the theoretical density. The sintering behavior was studied using dilatometry and thermogravimetric analysis coupled with mass spectrometry was also used. Sample microstructures were investigated using a scanning electron microscope.

## 4.2 *Results*

The influence of two major processing parameters, initial sample density  $\rho_o$  and heating rate  $\Omega$ , on the sintering behavior of MCMB was investigated. In all experiments, the maximum sintering temperature  $T_m$  was maintained constant at 1800 K. The following sample parameters were measured before and after heat treatment: initial and final mass ( $M_o$ ,  $M_f$ ), length ( $L_o$ ,  $L_f$ ), and diameter ( $D_o$ ,  $D_f$ ). Dynamic experiments were conducted to obtain sample length-time and mass-time profiles during sintering. The microstructures of initial samples and sintered materials were also investigated.

### 4.2.1 *Correlations Between Processing and Final Sintering Parameters*

For heating rate  $\Omega=1$  K/min, Figure 4.1 shows the dependences of relative changes in sample mass ( $\Delta M/M_o=M_f/M_o-1$ ), length ( $\Delta L/L_o=L_f/L_o-1$ ) and diameter ( $\Delta D/D_o=D_f/D_o-1$ ), as functions of initial density  $\rho_o$ . These parameters remain essentially constant over the range of investigated initial sample densities. It is also clear that the relative sample shrinkages in the radial and lateral directions are similar (~13%), and that sample mass decreases significantly (~12 %) during heat treatment.

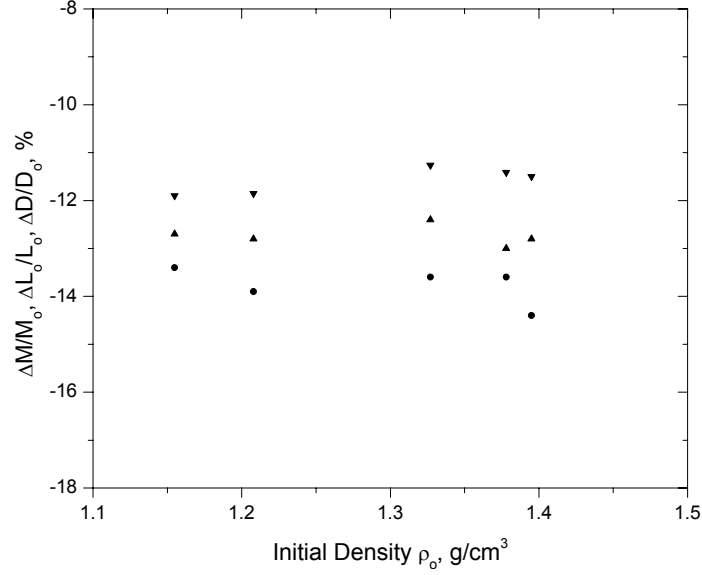


Figure 4.1: Changes in relative sample mass (●), length (▼), and diameter (▲) as functions of initial density;  $\Omega=1$  K/min

Based on the above, dependence of the sintered material's final density ( $\rho_f = 4M_f / \pi D_f^2 L_f$ ) versus  $\rho_0$  is presented in Figure 4.2. Note that the obtained data is described well by the linear relation  $\rho_f = 1.35\rho_0$  (curve 1), so that the sample density ratio,  $\rho_f/\rho_0$ , does not depend on  $\rho_0$  (curve 2).

To measure the theoretical density  $\rho^{pyc}$  of heat-treated compacted MCMB, several samples were specially preheated ( $\Omega=1$  K/min) to different temperatures in the range 400-1800 C. After conventional cooling, the samples were thoroughly crushed and their pycnometric densities were measured by the procedure described in Chapter 3. The evolution of  $\rho^{pyc}$  with temperature is illustrated in Figure 4.3. It increases with increasing temperature, from  $\rho_0^{pyc} = 1.48$  g/cm³ for initial powder to  $\rho_f^{pyc} = 1.98$  g/cm³ after heat treatment at  $T_m = 1800$  K. Note that  $\rho^{pyc}$  approaches the density of graphite ( $\sim 2.27$  g/cm³), which the material should reach at temperatures  $\sim 3200$  °C [Marsh and Rodriquez-

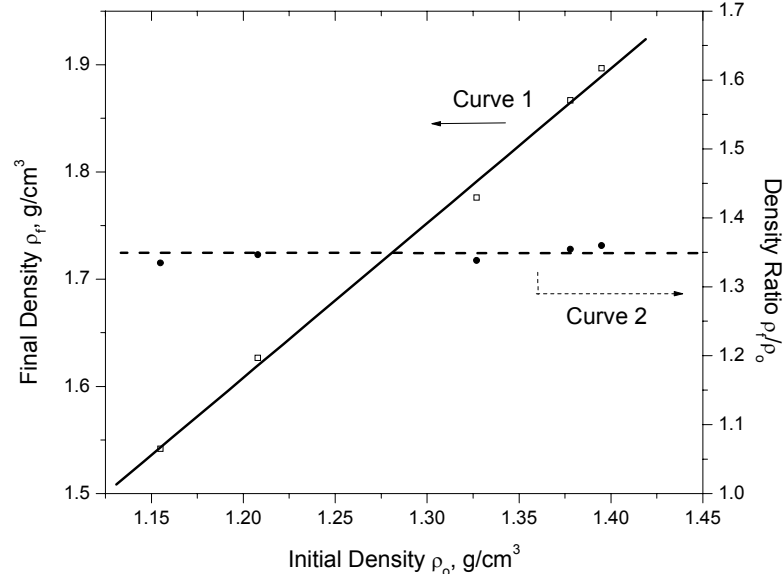


Figure 4.2: Dependence of final sample density as a function of initial density: (1)  $\rho_f$ , (2)  $\rho_f / \rho_0$ ;  $\Omega=1$  K/min

Reinoso, 2000]. It is interesting that the observed increase in pycnometric density starts at  $\sim 800$  K, while it remains essentially constant (Fig.4.3, stage 1) upon treatment at lower temperatures. Finally, after rapid change between 800-1200 K (stage 2), the rate of  $\rho^{pyc}$  increase slows at higher temperatures (stage 3).

Using the obtained data on theoretical densities, the dependence of sample final relative density,  $\rho_f^r$  [ $\rho_f^r = (4M_f/\pi D_f^2 L_f)/\rho_f^{pyc} = \rho_f / \rho_f^{pyc} = 1 - \varepsilon_f$ , where  $\varepsilon_f$  is the porosity of sintered material], as a function of initial relative sample density  $\rho_o^r$  [ $\rho_o^r = (4M_o/\pi D_o^2 L_o)/\rho_o^{pyc} = \rho_o / \rho_o^{pyc} = 1 - \varepsilon_o$ , where  $\varepsilon_o$  is the porosity of green sample] can be expressed (Figure 4.4). It is remarkable that the obtained data is described well by a linear relation with slope essentially equal to one.

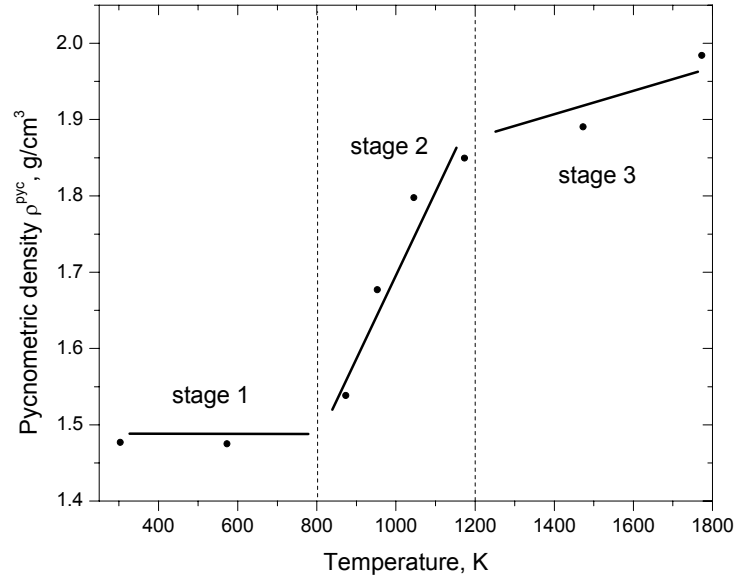


Figure 4.3: Sample pycnometric density,  $\rho^{pyc}$ , as a function of temperature

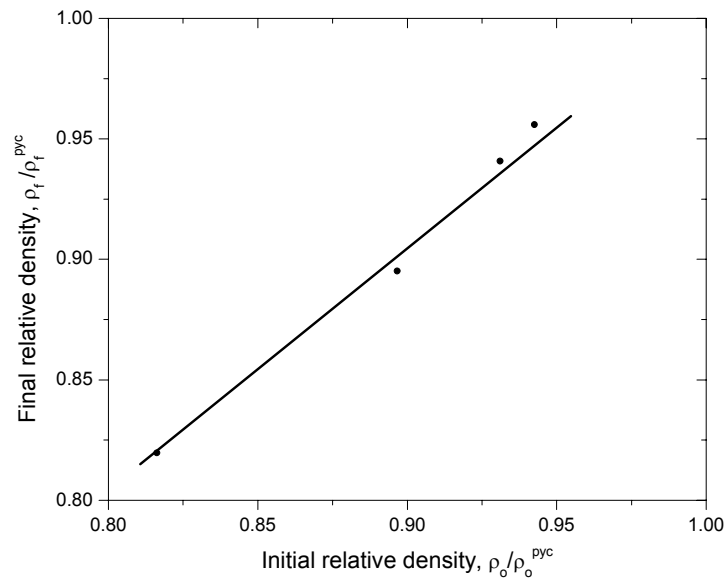


Figure 4.4: Final sample relative density as a function of initial relative density;  $\Omega=1$  K/min

As noted above, all data shown in Figures 4.1-4.4 were obtained using  $\Omega=1$  K/min. However, in the range of investigated  $\Omega$  values, all observed trends hold. For example (see Table 4.1), the change of sample mass ( $\Delta M/M_0$ ) is in the range 12-15 % and essentially independent of  $\rho_0$ . The ratio  $\rho_f/\rho_0$  lies between 1.31-1.36 for all  $\Omega$ , and since  $\rho_f^{\text{pyc}}/\rho_0^{\text{pyc}} = 1.98/1.48 = 1.34$ , this means that for all samples  $\rho_f^r \supset \rho_0^r$ . These results show that changing  $\rho_0$  or  $\Omega$ , while maintaining constant  $T_m$ , does not significantly influence the properties of the sintered materials.

TABLE 4.1

CHANGES OF RELATIVE SAMPLE MASS ( $\Delta M/M_0$ , %) AND DENSITY ( $\rho_f/\rho_0$ ) FOR DIFFERENT HEATING RATES AND INITIAL SAMPLE DENSITIES

Heating Rate, K/min	Initial Density g/cm <sup>3</sup>			
	1.15	1.21	1.31	1.38
0.3	$\Delta M/M_0 \sim -15\%$		-14	-13
	$\rho_f/\rho_0 \sim 1.31$		1.35	1.33
1	-12	-12	-11	-12
	1.33	1.34	1.34	1.36
5.5			-12	
			1.36	

#### 4.2.2 Dynamics of Sample Shrinkage

As described above, along with the static measurements performed on initial and final sample dimensions, the dynamics of its length change were investigated using a dilatometer. A typical experimental length-temperature profile is shown in Figure 4.5a. A polynomial fit ( $\Delta L/L_0 = F(T)$ ) was performed and used for further analysis of the shrinkage data. The process can be divided into different regions based on changes in the  $F'(T)$  function that describes the kinetics of length change (Figure 4.5b). The first three regions are alternating swelling and shrinking stages of relatively short duration and low rates. Distinctive shrinkage begins in region IV, which ends with a period of constant rate. The most significant transformations take place in the next region (V), characterized by a steadily increasing shrinkage rate, which reaches a maximum at  $\sim 1000$  K. It is interesting that while temperature increases in region VI, shrinkage rate gradually decreases.

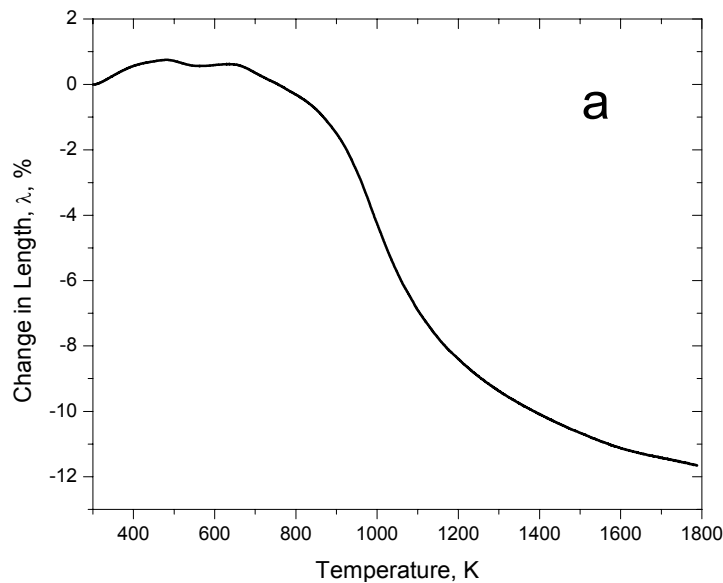


Figure 4.5 a: Typical sample shrinkage during sintering as a function of temperature

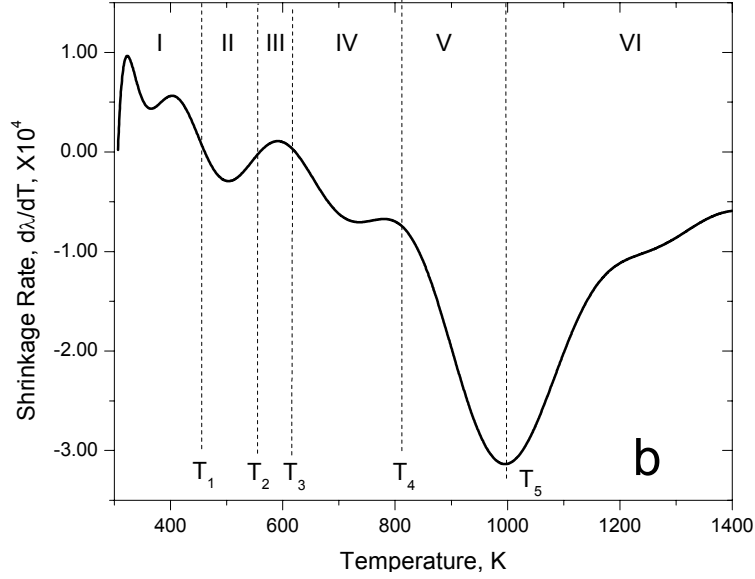


Figure 4.5 b: Typical sample shrinkage rate during sintering  $d\lambda/dT$ ;  $\Omega=1$  K/min

All of the regions noted above (I-VI) were observed for the entire range of investigated sample initial densities and heating rates. The characteristic temperatures  $T_i$  (Figure 5b) and swelling/shrinkage rates do not depend on  $\Omega$ , but are influenced by  $\rho_o$  (see Table 3). Specifically, increase in  $\rho_o$  shifts the initial regions (II-IV) to higher temperatures, while the temperature range (800-1000 K) and shrinkage rate ( $3 \cdot 10^{-4} \text{ K}^{-1}$ ) for the vital region (V) remain essentially unchanged.

#### 4.2.3 Dynamics of Mass Loss During Sintering

As shown in Figure 4.1, significant reduction of mass occurs along with the decrease of sample dimensions during heat treatment of compacted MCMB in an inert atmosphere. To investigate this effect in detail, TGA / MS was conducted and the typical results are shown in Figure 4.6. From the mass loss kinetics (Figure 4.6a), three distinct events ( $\sim 500$ , 800, and 1000 K) may be identified. In Figure 4.6b, it is seen that the evolution of gas with 91 AMU contributes to the first peak (500 K) while that with 16

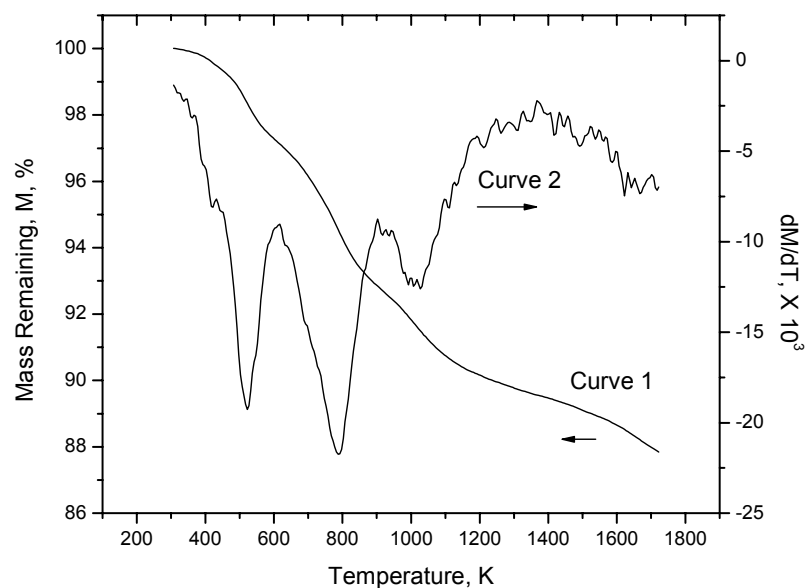


Figure 4.6 a: Results of thermogravimetric and mass spectrometry analysis; mass loss and rate of mass loss

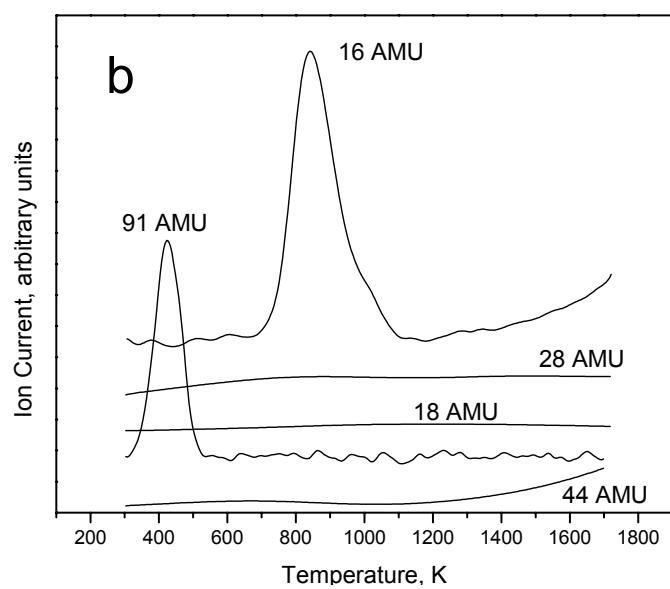


Figure 4.6 b: Results of thermogravimetric and mass spectrometry analysis; evolution of different gas species



AMU (i.e.  $\text{CH}_4$ ), to the second (800 K). Note that there are no peaks for the evolution of water (18), carbon monoxide (28), and carbon dioxide (44).

#### 4.2.4 *Microstructural Transformations*

The typical microstructures for compacted initial as well as heat-treated samples are shown in Figure 4.7. It can be seen (Figure 4.7a and b) that the initial size distribution is bimodal, with large particles ( $\sim 10\ \mu\text{m}$ ) forming a framework within the sample and smaller beads ( $\sim 1\ \mu\text{m}$ ) essentially filling the remaining volume. After heat treatment (Figure 4.7c and d), one can observe classical sintering necks between the particles.

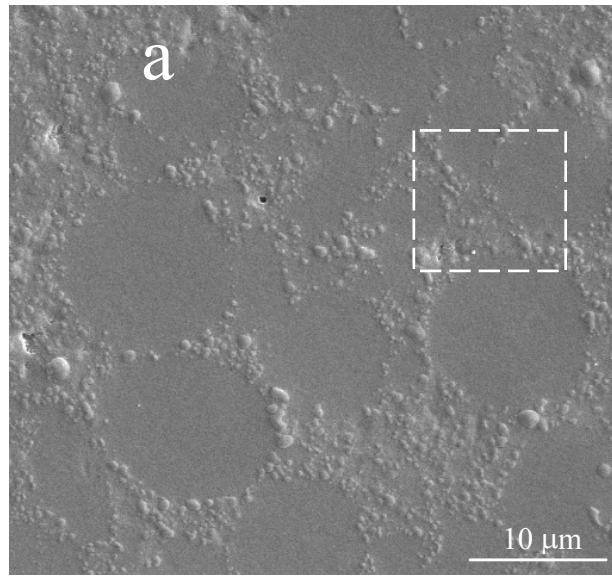


Figure 4.7 a: Typical microstructure of initial MCMB compacts.

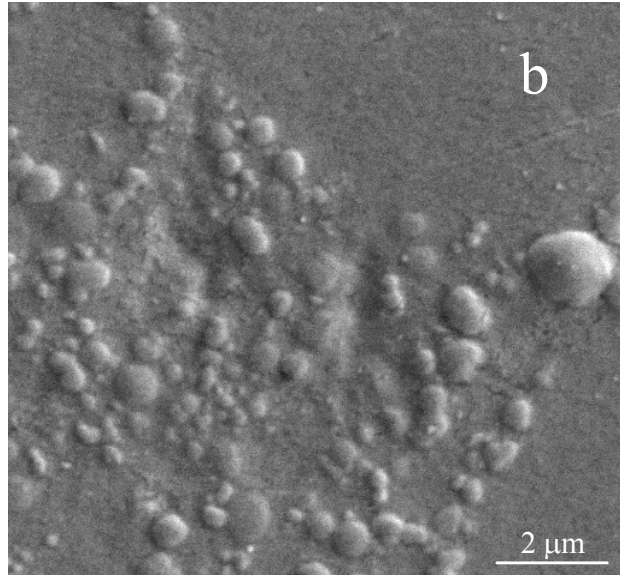


Figure 4.7 b: An expanded version of the rectangle shown in Figure 4.7a

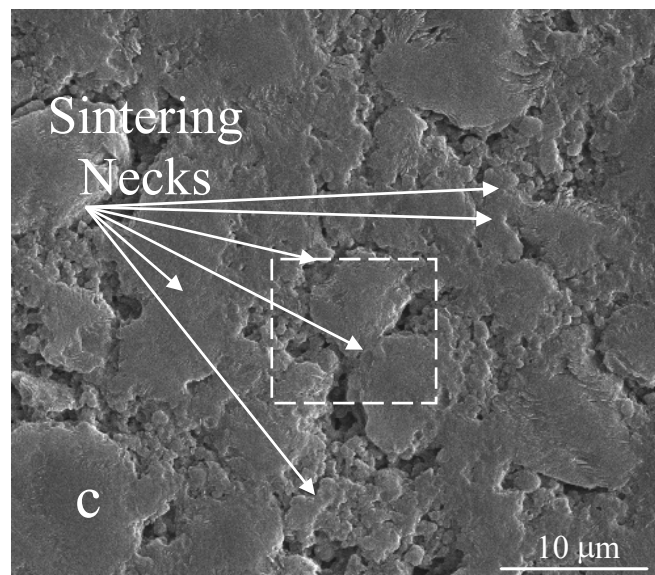


Figure 4.7 c: Typical microstructure of sintered MCMB.

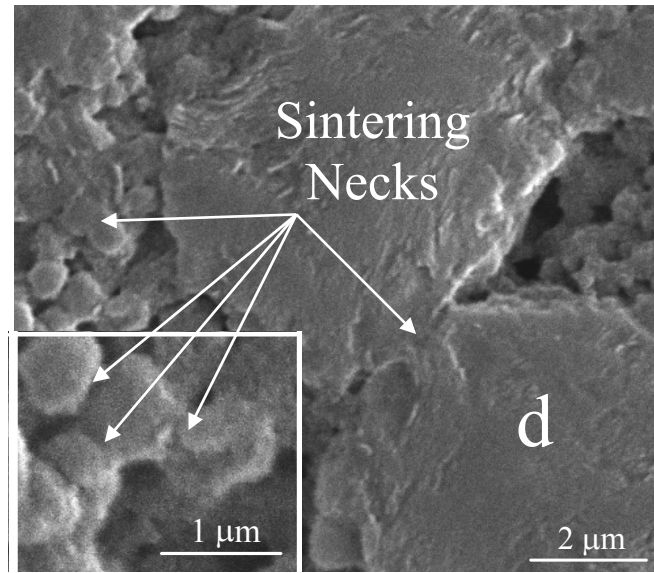


Figure 4.7 d: An expanded version of Figure 4.7 c

### 4.3 Discussion

The discussion begins with an analysis of shrinkage and mass loss kinetics to identify characteristic regions of the sintering process, followed by a combined analysis of the dynamic and overall results to explain the unique sintering behavior of MCMB.

#### 4.3.1 Shrinkage Kinetics

It can be seen that for the investigated MCMB, there is a temperature range 800 - 1200 K in which the shrinkage rate is exceptionally high (see Figure 4.5b). Note that this region exists over the same temperature values and reaches a consistent maximum shrinkage rate over all processing conditions studied (see Table 4.2). Additionally, it is clear that further increases in temperature lead to a decrease in the shrinkage rate (region VI). The above unusual behavior requires an explanation.

TABLE 4.2

## SINTERING PARAMETERS FOR DIFFERENT INITIAL SAMPLE DENSITIES

Initial Density, g/cm <sup>3</sup>	Characteristic Temperature, K					Maximum Shrinkage Rate x10 <sup>4</sup> , K <sup>-1</sup>				
	T <sub>1</sub>	T <sub>2</sub>	T <sub>3</sub>	T <sub>4</sub>	T <sub>5</sub>	I	II	III	IV	V
1.15	460	560	610	790	1000	-0.09	0.3	-0.6	0.8	3.2
1.38	530	600	680	825	990	-1.4	0.5	-0.8	0.8	3.2

One way to gain additional insight into the mechanism which gives rise to these various sintering stages is to characterize the *effective activation energy* of the sintering process by using a well-established procedure [Rahaman, 1995; German, 1996; Perez-Maqueda et al., 2002]. Note that the main purpose in following this general analysis is to *qualitatively* identify differences between the various regions, rather than to quantitatively calculate the effective activation energy values.

Briefly, for uniform spheres, neck growth is represented by

$$\left(\frac{x}{r}\right)^n = \frac{Bt}{r^m} \quad (4.1)$$

where  $x$  is neck radius,  $r$  is particle radius,  $t$  is time, and  $m$  and  $n$  are constants that depend on the kinetic mechanism. Note that the factor  $B$  is temperature dependent, with a relationship given by

$$B = B_0 T^a e^{-Q/RT} \quad (4.2)$$

where  $T$  is temperature,  $Q$  is activation energy,  $B_0$  is a factor that collects material and numerical constants, and  $a$  is a parameter that also depends on the kinetic mechanism.

Further, if sintering occurs due to neck formation as a result of bulk diffusion, then the sample shrinkage and neck formation are related by [German, 1996]

$$\lambda = \frac{\Delta L}{L_0} = \left( \frac{x}{2r} \right)^2 \quad (4.3)$$

where  $\lambda$  represents the dimensionless shrinkage. Combining equations 4.1 – 4.3 for linear heating rate processes, we obtain

$$\frac{d(\ln \lambda)}{d(\ln T)} = \frac{2(a+1)}{n} + \frac{2Q}{Rn} \cdot \frac{1}{T} \quad (4.4)$$

which relates sample shrinkage to the effective activation energy,  $Q$  of the sintering process.

Note that  $Q$  cannot be separated from the kinetic parameter,  $n$ . Nevertheless, to examine transitions between sintering stages, one can use the ratio  $Q/n$ , obtained as the *slope* when the left hand side is graphed as a function of  $1/T$ . A typical result of this analysis is shown in Figure 4.8 (curve 1), where the shrinkage rate (curve 2) is also shown to aid in identifying the shrinkage regions.

It can be seen that especially in the region of low (IV) temperature, the effective activation energy is high. Remarkably, the intermediate temperature region (V) has essentially no barrier to the shrinkage process, as the effective activation energy approaches zero. This is an unexpected result, since densifying processes are typically thermally activated [German, 1996]. Thus the sintering mechanism considered above is

not valid, and an alternative one is required to explain the observed rapid shrinkage behavior.

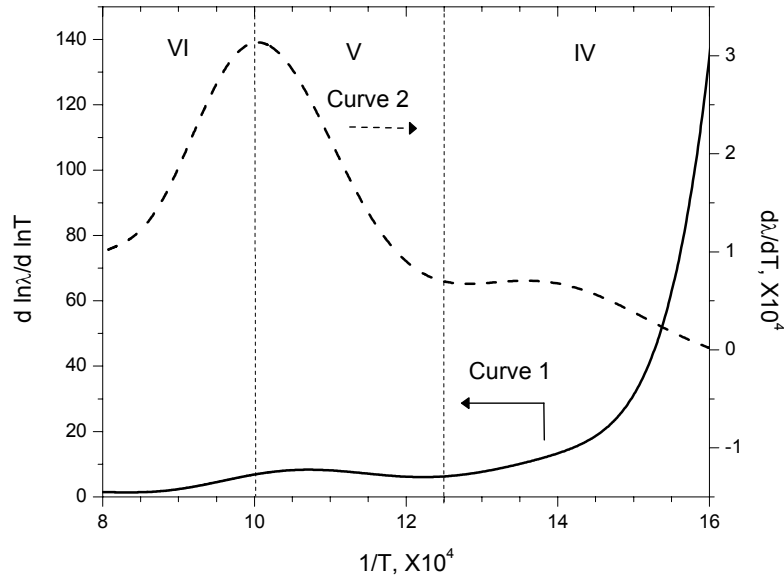


Figure 4.8: Activation energy analysis of different shrinkage regions

#### 4.3.2 Mass Loss Analysis

From the association between the swelling observed in region I (Figure 4.5b) and the peak in the evolution of 91 AMU gas (Figure 4.6b), it may be concluded that this swelling is caused by gas release and not the relief of molding stress, as previously suggested [Hoffmann and Hüttinger, 1994]. Further, from the position of the second mass loss peak (800 K, Figure 4.6a) which corresponds to methane (Figure 4.6b), it appears that this marks the carbonization of the  $\beta$ -resin, which is believed to be responsible for the liquid phase sintering [Martinez-Escandell et al., 1999]. During heat treatment, the  $\beta$ -resin experiences a viscosity decrease [Gao et al., 2002], allowing it to flow and form necks between particles, as observed in Figures 7c and d. Finally, Figure 4.9 shows that the maximum peak in shrinkage (1000 K) occurs after the carbonization of

the  $\beta$ -resin, indicating that viscous phase sintering cannot be responsible for the observed high densification rate. However, the third mass loss event (1000 K) corresponds to the maximum in shrinkage rate, indicating that the process controlling this stage also involves gas evolution. Because mass spectrometry was conducted for all species in the range 10 - 300 AMU, it is concluded that this peak corresponds to hydrogen gas (2).

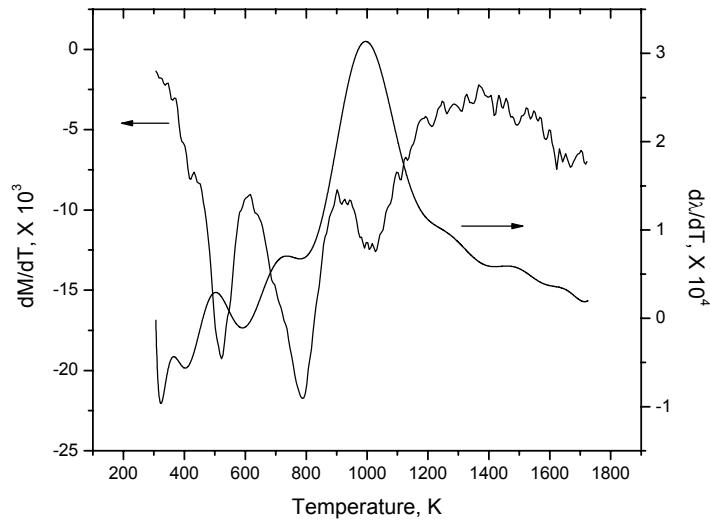


Figure 4.9: Rates of mass loss and shrinkage

#### 4.3.3 *Microstructural Transformations*

As seen in Figures 4.7c and d, the spherical shape of the microbeads is largely unaltered by the sintering process. However, the particles become connected, and the irregular shape of larger microbeads is attributed to neck formation between large and small spheres. Statistical analysis of the obtained microstructures shows that the average particle diameter reduction for large beads was  $\sim 20\%$ .

#### 4.3.4 Overall Shrinkage Model

As seen in Figures 4.1 and 4.2 and Table 4.2, the results of the overall heat treatment process ( $\Delta M/M_o$ ,  $\Delta D/D_o$ ,  $\Delta L/L_o$ , and  $\rho_f/\rho_o$ ) are unaffected by changes in either  $\rho_o$  or  $\Omega$ , when  $T_m$  is held constant (1800 K). Under these conditions, the ratio  $\rho_f/\rho_o$  remains constant at  $\sim 1.35$ . Simultaneously, independent measurements of the theoretical density through pycnometry show that the ratio  $\rho_f^{pyc}/\rho_o^{pyc}$  is also  $\sim 1.35$ . Hence the ratio of the final to initial relative density  $\rho_f^r/\rho_o^r \sim 1$  for all investigated processing conditions, which means that the sample porosity also remains unchanged.

All of the above considerations lead to the conclusion that the MCMB shrinkage process can be explained mainly by changes in theoretical density of the microbeads, while maintaining cohesion between the particles. This is illustrated this by a simple example. Assume that initially there are two spherical particles in contact with each other (Fig. 4.10a) of radius  $r_o$  (thus length of the “sample” is  $L_o=4r_o$ ), mass  $M_o$  and theoretical density  $\rho_o^{th} = 3M_o/4\pi r_o^3$ . Such a cylindrical “sample” has initial density  $\rho_o = 2M_o/L_o\pi r_o^2 = M_o/2\pi r_o^3$ . Further, assume that the *only* process which occurs is the change in theoretical density to  $\rho_f^{th}=3M_f/4\pi r_f^3$ , while the contact point remains the same (Fig. 4.10b). The final density of such a sample equals  $\rho_f = M_f/2\pi r_f^3$ . In this case, indeed, the ratio between theoretical densities  $\rho_f^{th}/\rho_o^{th} = (M_f/M_o)(r_o/r_f)^3$  exactly equals the ratio of sample densities  $\rho_f/\rho_o = (M_f/M_o)(r_o/r_f)^3$ , and thus sample porosity remains constant. In other words, it appears that if the mass of each particle decreases by 12 % (Figure 4.1) and its pycnometric density increases by a factor of 1.35 (Fig. 4.3), then the change in sample length should be  $\sim 13$  %, which is very close to the experimental result (Fig.4.1).



Note that all above parameters (i.e. mass, length and theoretical density) were measured *independently*.

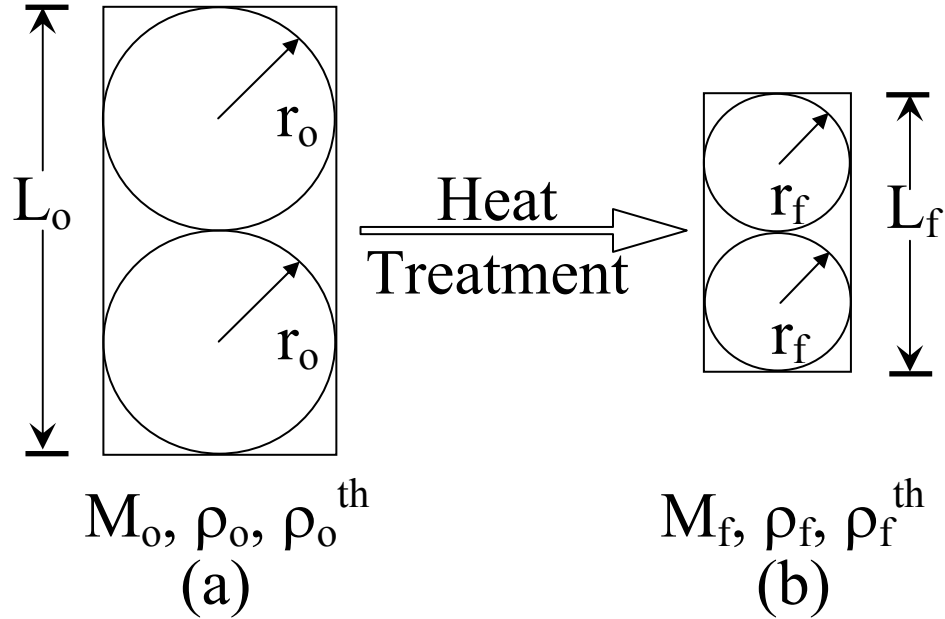


Figure 4.10: A schematic to illustrate the effect of increasing theoretical density on sample shrinkage

Further, this model can be used to estimate the instantaneous shrinkage, which can then be compared with the dilatometric results.

Sample shrinkage  $\lambda$  can be written as

$$\lambda_i = \frac{L_i - L_o}{L_o} = \frac{L_i}{L_o} - 1 \quad (4.5)$$

where  $\lambda_i$  and  $L_i$  are the dimensionless sample shrinkage and sample length at state i.

The relative densities of the initial and final samples can be represented by

$$\rho_o^r = \frac{m_o^{MB} / \rho_o^{MB}}{V_o} = \frac{m_o^{MB} / \rho_o^{MB}}{L_o^3} \quad (4.6)$$

$$\rho_i^r = \frac{m_i^{MB} / \rho_i^{MB}}{V_i} = \frac{\Delta_i m_o^{MB} / \rho_i^{MB}}{L_i^3} \quad (4.7)$$

where the subscripts o and i refer to the original and state i, respectively,  $\rho_o^r$  and  $\rho_i^r$  are the relative densities of the sample,  $V_o$  and  $V_i$  are the sample volumes,  $m_o^{MB}$  and  $m_i^{MB}$  are the sample MCMB mass,  $L_o$  and  $L_i$  are the sample lengths, and  $\rho_o^{MB}$  and  $\rho_i^{MB}$  are the theoretical densities of the MCMB. The variable  $\Delta_i$  describes the fraction of the original mass remaining at state i, so that  $m_i^{MB} = \Delta_i m_o^{MB}$ . It has been shown that the relative sample density remains constant during heat treatment to 1800 K, thus we may assume that  $\rho_o^r = \rho_i^r$ . Substituting Equations 2 and 3 into Equation 1, it can be shown that

$$\lambda_i = \left( \frac{\rho_o^{MB}}{\rho_i^{MB}} \right)^{1/3} \Delta_i^{1/3} - 1 \quad (4.8)$$

which only requires descriptions of theoretical density and mass loss behavior during changing temperature to allow estimation of dilatometric results. These descriptions were obtained by fitting data shown in Figures 4.3 and 4.6a. The results are shown in Figure 4.11, which compares the expected and actual shrinkage rates. It is clear that the calculated and measured shrinkage rates are similar, with some exceptions. First, the model employed to develop the estimated shrinkage does not account for swelling effects which are known to be present. Therefore, it is not surprising that there are marked differences between the two curves at low temperatures, where sample swelling is observed. Second, although the maximum in shrinkage rate is observed in both cases, the calculated maximum occurs about  $\sim 50$  °C before the observed one. This is likely an artifact of the model's inability to account for swelling. In any case, a match with only

50 °C error may be considered good from such a simple model. Finally, the high temperature behavior of the model erroneously predicts a broad minimum in the shrinkage rate, however, it does capture the decrease in the shrinkage rate observed in the experimental data. In conclusion, it is remarkable that such a simple model predicts the shrinkage of the pure MCMB system using only the changes of mass and pycnometric density as the two independently measured variables.

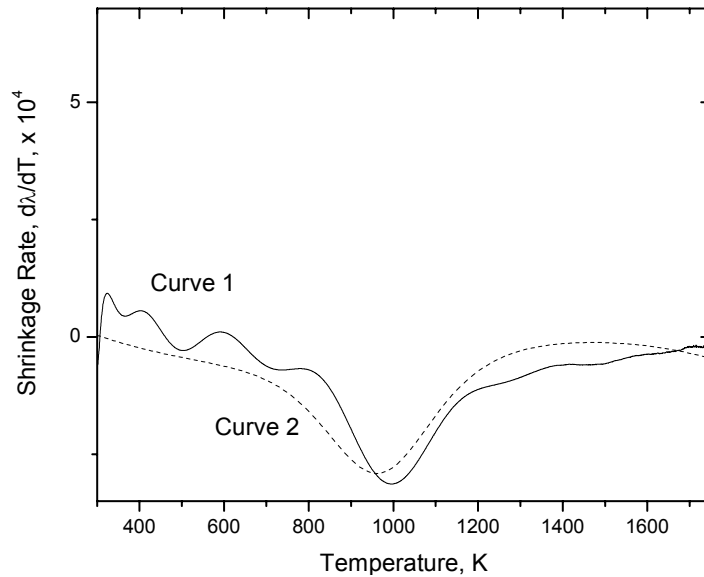


Figure 4.11: Comparison of expected and observed dilatometric results for pure MCMB.  
— (Curve 1): observed shrinkage rate, ----(Curve 2): expected shrinkage rate

#### 4.4 *Densification Mechanism*

A densification mechanism for the investigated MCMB can now be formulated, which consists of two important processes: neck formation between particles as a result of a non-densifying liquid-phase sintering mechanism at temperatures < 800 K, and rapid sample shrinkage due to changes of theoretical particle density resulting from crystallographic rearrangement in the temperature region 800 – 1200 K.

Based on the prior literature and the present work, it appears that the sintering necks are formed by the  $\beta$ -resin and its subsequent carbonization ( $< 800$  K) by a viscous phase non-densifying sintering mechanism. These necks assure continued particle-to-particle contact required by the simple model discussed in Section 4.4, where the increase in theoretical density is responsible for the observed significant shrinkage. Note that this process does not have any relation to the conventional solid state sintering mechanism as suggested previously [Hoffmann and Hüttinger, 1994; Gao et al., 2002]. Indeed, as evidenced by Figure 4.8 and discussed in Section 4.3.1, the activation energy analysis suggests that there is no densifying sintering mechanism, such as solid state sintering, present during the period of intensive shrinkage.

Crystallographic transformations can readily lead to changes in material theoretical density. A decrease in the graphene layer spacing, observed in other studies (1, 9, 11), may explain the increased theoretical density (Figure 4.3) and the decreased particle size (see Section 4.3.3). Also, hydrogen gas evolution during this stage is consistent with the perfection of the lattice structure. Further investigations are currently underway to provide additional support for this mechanism.

#### **4.5 Conclusion**

The ultimate goal of this work is to advance the technology required for the rapid, low-cost processing of MCMB to carbon-based high performance materials. In this context, understanding the MCMB sintering mechanism is an important step towards optimization of the matrix prior to introducing the reinforcing elements. Indeed, it is well

known that porosity and microstructure are important factors in determining the mechanical properties of composite materials.

The proposed sintering mechanism suggests that to achieve a product with lowest porosity and optimum microstructure, several recommendations should be followed: (i) prepare green samples with highest initial density; (ii) avoid crack formation during heat treatment by identifying optimum temperature-time schedule; (iii) minimize sample mass loss while maintaining large changes in pycnometric density. Based on these rules, materials with relative porosity ~8 % and uniform microstructure in the first stage of sintering (up to 1800 K) have been produced. Further work, currently in progress, will demonstrate if pore-free pure carbon can be obtained following a second high-temperature (up to 2500 K) stage.

## CHAPTER 5

### HIGH-TEMPERATURE SINTERING AND GRAPHITIZATION

As noted in Chapter 2, mesocarbon microbeads are a special type of carbon with extraordinary sintering characteristics at relatively low temperatures. It is possible that unique high temperature sintering mechanisms may also be present. These processes would co-exist with graphitization, which may be related to the physical properties as in carbon fiber systems [Fitzer and Manocha, 1998]. Additionally, some question remains concerning the kinetics and mechanism of graphitization. This chapter is focused on determining the presence of any high temperature sintering mechanisms and studying in detail the kinetics of graphitization in MCMB.

#### **5.1 *Experimental Methods***

As stated previously, the properties of polyaromatic mesophases depend on the manufacturing, extraction, and pretreatment procedures, but all of them possess the ability to self-sinter at relatively low temperatures. Investigation of one type of commercially available mesocarbon microbeads (Osaka Gas, Japan), whose

characteristics are summarized in Table 3.1, is reported. The MCMB were calcined prior to heat treatment by graphite resistance furnace, described in Chapter 3.

### **5.1.1 Sintering**

The material was uniaxially compacted in a 31 mm cylindrical die at pressures about 60 MPa with a dwelling time of 9 minutes. As the focus of this study is the high-temperature behavior of the material, all samples were presintered with heating rate  $W = 1$  K/min to 1800 K prior to final heat treatment. Samples were then processed at a constant heating rate to the desired temperature in the range 1900 – 2800 K, with no isothermal period, except where indicated. In studying the sintering behavior,  $W$  was varied to determine the effect on the process variables, i.e., mass loss, shrinkage, and the evolution of the theoretical and relative density. However, the obtained results show little dependence on the heating rate, and the variation is well within the experimental scatter. The data do show a relationship with the heat treatment temperature (HT), and thus is presented without indication of the heating rate used.

After sintering, helium pycnometry was used to measure the true material density. For microstructural examination, several samples were compacted at 300 MPa, increasing the relative green density to 94%. The effect of sintering on pore microstructure was investigated via SEM.

### **5.1.2 Graphitization**

Isothermal graphitization studies were conducted on MCMB powder placed in a graphite crucible and heat treated. These samples were processed at 25 K/min to within

~200 K of the required graphitization temperature, then stepped to the desired value and held for the specified time. Experiments were conducted at five graphitization temperatures,  $GT = 2500, 2600, 2700, 2750, \text{ and } 2800 \text{ K}$ , and for six graphitization times,  $Gt = 20, 30, 60, 180, 300, \text{ and } 900 \text{ minutes}$ . In addition, for  $GT = 2800 \text{ K}$ , the longest graphitization time used was  $Gt = 1200 \text{ minutes}$ . These isothermal experiments are of the type most commonly conducted in graphitization studies [Pacault, 1971]. In all cases, x-ray diffraction patterns were collected and the interlayer spacing  $d_{002}$  was determined, as described in Chapter 3.

## **5.2 Results**

### **5.2.1 Sintering**

The effect of HT on changes in sample mass and length are shown in Figures 5.1 and 5.2, respectively. It can be seen (Figure 5.1) that the largest change in mass (~12%) occurs at temperatures below 1800 K (Stage I) [for details see Chapter 4] while at  $HT > 1800 \text{ K}$  *essentially no mass change was observed* (Stage II). Similarly, the majority of length changes occur during low-temperature treatment ( $T < 1800 \text{ K}$ ; Stage I). The shrinkage rate decreases significantly (~ 10 times) during sintering at  $HT > 1800 \text{ K}$  (Figure 5.2; Stage II). Note that shrinkage occurs isotropically, i.e. it is essentially the same in all directions. Also, for these experiments the final sample porosity was ~ 20%. Thus the decreasing shrinkage rate with increasing temperature cannot be explained by approaching the limit of theoretical density.



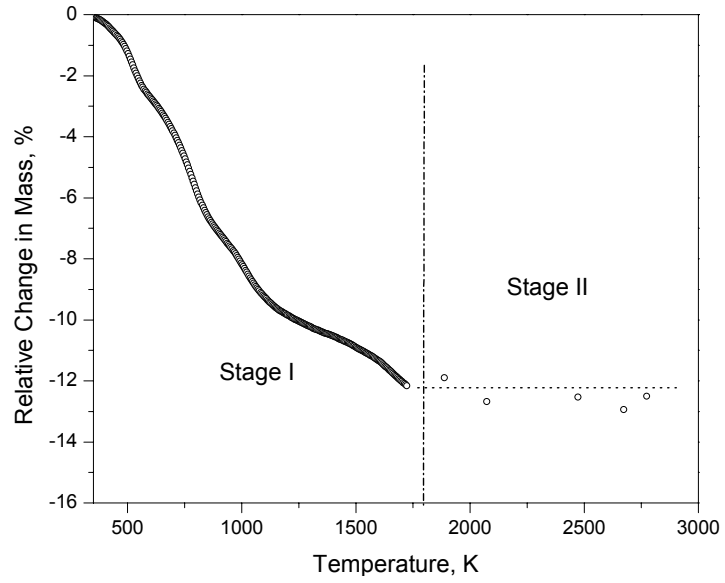


Figure 5.1: Relationship between heat treatment temperature and relative change in mass

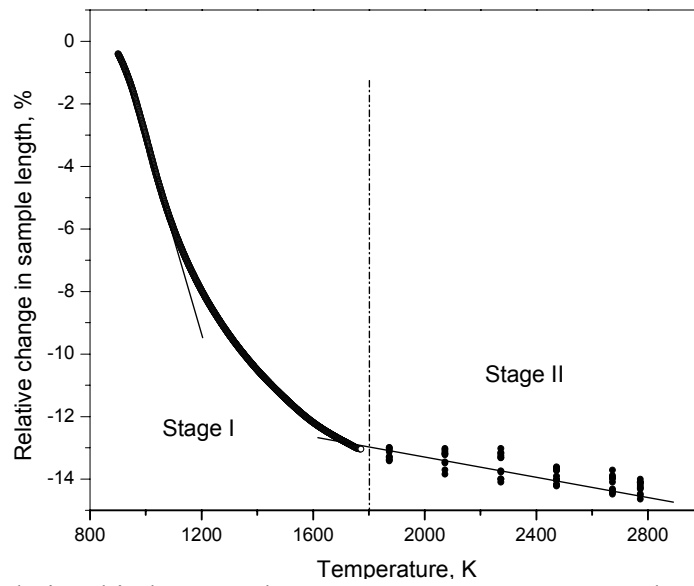


Figure 5.2: Relationship between heat treatment temperature and relative change in length

As mentioned above, helium pycnometry was used to measure the true material density. The results are shown in Figure 5.3. It can be seen that pycnometric density,  $\rho_{\text{pyc}}$ , rises sharply in the temperature range 800 – 1500 K, as was observed in Chapter 4, and at  $T > 1800$  K continues to increase slowly, reaching  $\sim 2.1 \text{ g/cm}^3$  at  $\text{HT} = 2800$  K. This value is expected to increase further with increasing HT to  $2.26 \text{ g/cm}^3$ , corresponding to graphite. Using  $\rho_{\text{pyc}}$  as a measure of the material theoretical density, the relative sample densities were calculated (see Figure 5.4). It is shown that the relative density remains essentially constant over a wide range of HT. Note that such behavior was also observed for lower heat treatment temperatures in the range of 500 – 1800 K, described in Chapter 4.

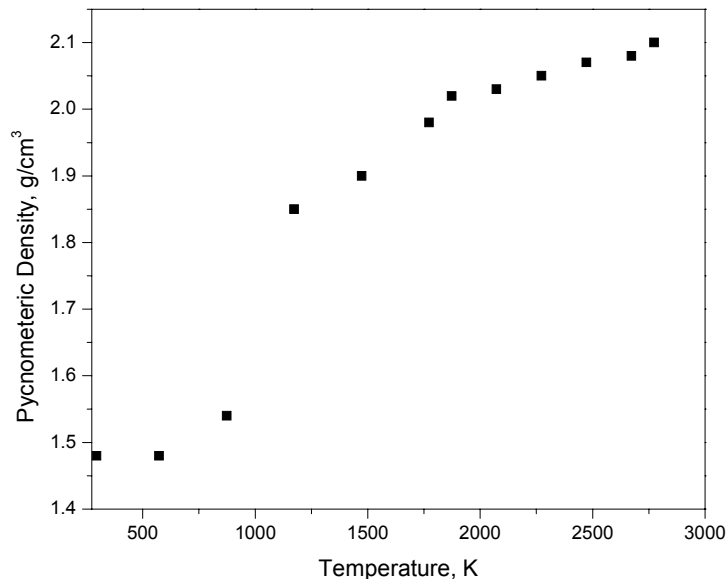


Figure 5.3: Evolution of pycnometric density with heat treatment temperature

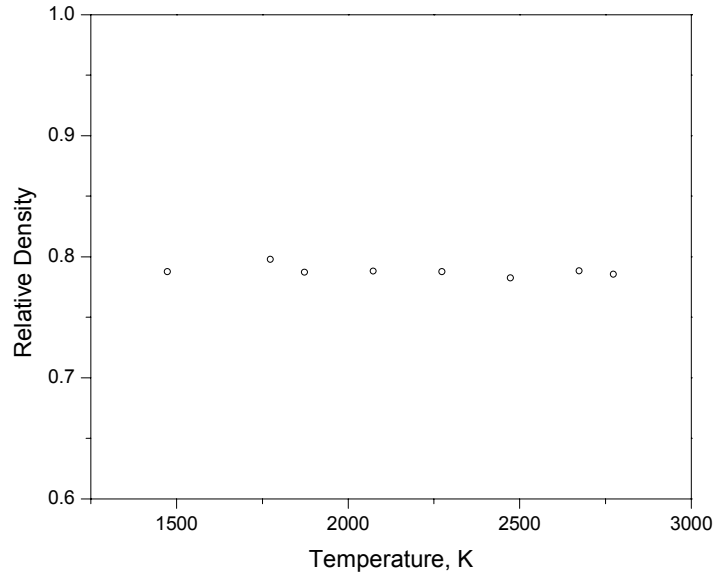


Figure 5.4: Dependence of relative density on heat treatment temperature

### 5.2.2 *Microstructure*

Typical microstructures of samples with high relative density  $\sim 94\%$  heat-treated under different conditions are shown in Figure 5.5; Figure 5.5 a shows a sample heat treated at 1 K/min to 1800 K, while 5.5 b shows the same sample after heat treatment at 2800 K for 50 hours. Changes in the pore microstructure induced by increased heat treatment can be observed. Specifically, the number of small pores decreases and the size of large pores increases.

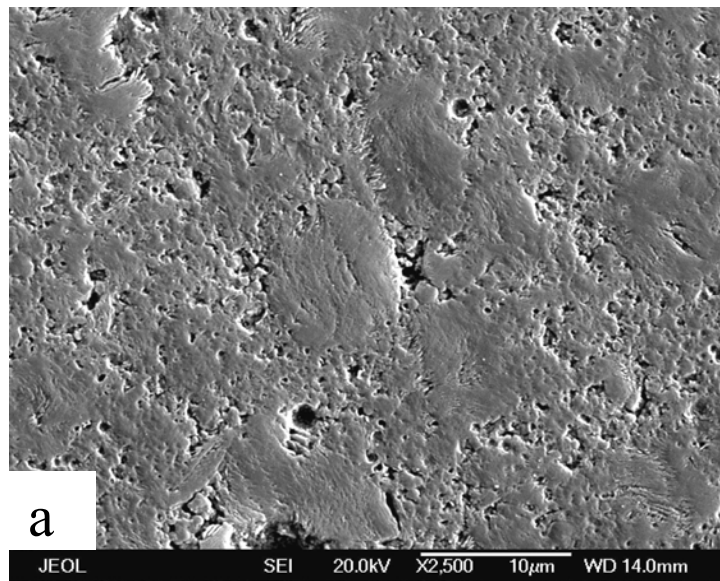


Figure 5.5 a: Typical microstructure for a sample heat treated to 1800 K

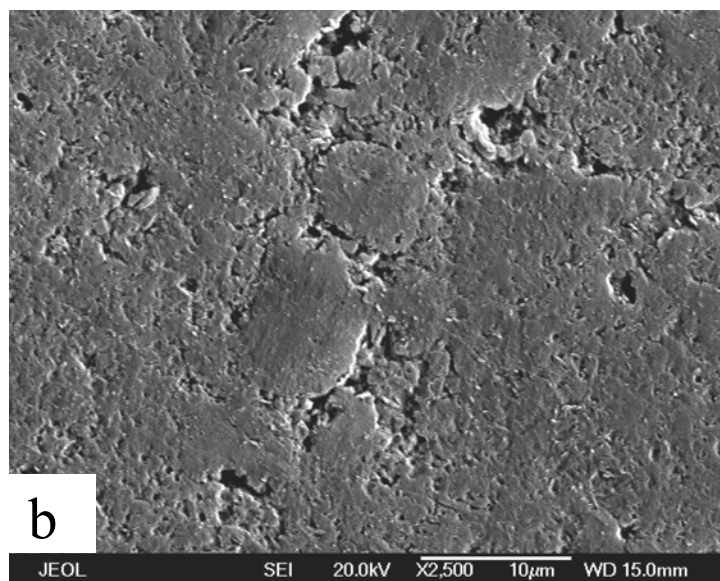


Figure 5.5 b: Typical microstructure for a sample heat treated to 2800 K for 50 hours

### 5.2.3 Graphitization

Graphitization is an important material parameter which can be related to performance [Fischbach, 1971]. To investigate the kinetics of graphitization in MCMB, the change of interlayer spacing  $d_{002} = c/2$  during isothermal heat treatment at various GT (2500, 2600, 2700, 2800 K) and Gt (20 to 1200 minutes) was monitored, as shown in Figure 5.6. It can be seen that both the temperature and time influence the graphitization rate. Note that while the minimum observed layer spacing is 3.367 Å, it is expected that, given sufficiently long graphitization times, the value for MCMB would approach that of graphite (3.354 Å).

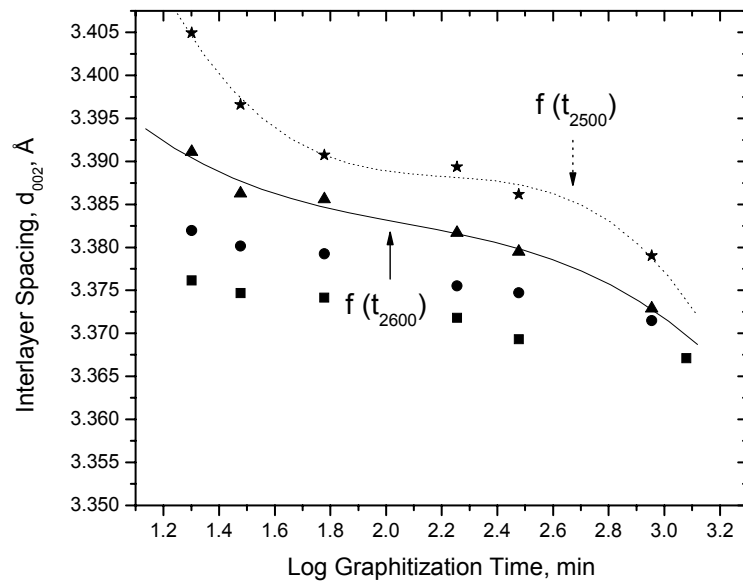


Figure 5.6: Graphitization kinetics at various temperatures;

★ - 2500 K, ▲ - 2600 K, ● - 2700 K, ■ - 2800 K

### 5.3 *Discussion*

#### 5.3.1 *Sintering*

It has been shown previously (Chapter 4) that the low temperature ( $< 1800$  K) sintering proceeds in two main stages: (i) neck formation between particles by a viscous phase non-densifying sintering mechanism ( $< 800$  K); (ii) rapid sample shrinkage due to changes of true particle density in the temperature range  $800 - 1200$  K. However, this significant shrinkage does not lead to decrease of the total material porosity. In general, it may be possible to decrease total porosity as the result of a volume vacancy diffusion mechanism, but it is known that this process proceeds at measureable rates only at temperatures on the order of 70% of the material melting point [German, 1996]. Since the melting point of carbon is  $> 3773$  K [Green, 1997], porosity decreases by this mechanism are not expected.

The work reported in this chapter is meant to illuminate any possible densifying sintering mechanisms which may be active at higher temperatures. Figure 5.4 shows that the relative density of the material remains constant during heat treatment up to  $HT = 2800$  K. Indeed, these heat treatments produce further increases in bulk density, but corresponding increases in pycnometric density (up to  $2.134 \text{ g/cm}^3$ ) caused no change in sample porosity.

These observations are supported by the microstructures. While estimates show that microstructural changes due to diffusion over this relatively short period (50 hours) will be small, the effect of sintering on this system can be delineated. First, increasing

HT and the heat treatment time decreases the number of small pores and increases the size of large pores (Figure 5.5). Additionally, by eliminating small pores, the density of regions away from the large pores is increased. Finally, analysis shows that the fraction of these dense regions increases with increasing HT. These transformations can be explained within the framework of conventional diffusion-based solid state sintering mechanisms [Whittemore and Varela, 1980]. It is well known that in the first stages of this process, large pores grow at the expense of small pores [German, 1996]. During later stages, it may be possible for these pores to diffuse to the sample surface, decreasing total porosity.

### 5.3.2 *Graphitization*

The isothermal data shown in Figure 5.6 can be used to estimate the activation energy of the graphitization process. The procedure was described in detail elsewhere [Lachter et al., 1986] and is briefly outlined here. The isotherms at 2500 and 2600 K are used as an example. A polynomial is used to fit each isotherm; in this work, third order polynomials were used. These polynomials describe the relationship between  $d_{002}$  spacing and graphitization time, and are referred to as  $y=f(t_{2500})$  and  $y=f(t_{2600})$ . The values of  $d_{002}$  spacing which are common to both isotherms are defined as the overlap interval. This interval for the 2500 and 2600 K isotherms is 3.379-3.391 Å, representing the smallest and longest time at 2600 K and 2500 K, respectively. The overlap interval is divided into a large number of points, in this work taken as 50. The fit lines  $y=f(t_{2500})$  and  $y=f(t_{2600})$  are then used to find the values of time that correspond to each of the specified points in the overlap interval. These two sets of time values are referred to as

$X_{2500}$  and  $X_{2600}$ . The temperature of one isotherm is chosen as the reference,  $T_R$ , and in this work 2500 K was selected. A constant  $\Delta$  is added to all points in the set  $X_{2600}$ , which is chosen to minimize the sum of the square of the differences between  $X_{2500}$  and  $(X_{2600} + \Delta)$ . By adding  $\Delta$ , the isotherm at 2600 K is essentially shifted to best line up with that at  $T_R$ . This procedure is followed for all isotherms, and the resulting master curve shown in Figure 5.7 indicates that the data can be superposed by translations along the time axis.

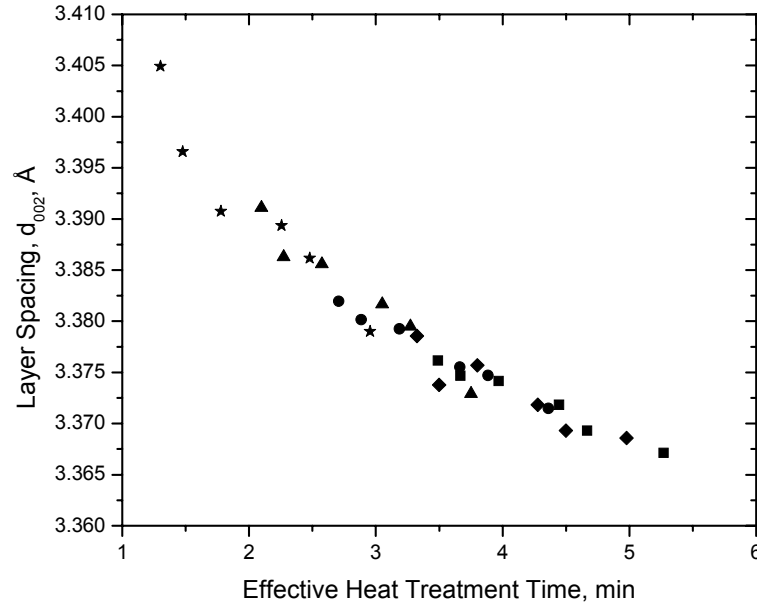


Figure 5.7: Master curve showing relationship between  $d_{002}$  layer spacing ...and effective heat treatment time; ★ - 2500 K, ▲ - 2600 K, ..... ● - 2700 K, ◆ - 2750 K, ■ - 2800 K

By superposing isothermal curves, it is assumed that the activation energy is constant with temperature. The fact that the superposition of these curves results in a single curve of reasonable quality supports this assumption [Fishbach, 1971]. The shifts which make this superposition possible can then be related to the activation energy by the



following analysis. Superposing an isotherm at temperature  $T$  onto an isotherm at  $T_R$  requires a shift given by [Lachter et al., 1986]

$$\Delta = \log \left( \frac{k(T)}{k(T_R)} \right) = \left( \frac{-Q}{R} \right) \left( \frac{1}{T} - \frac{1}{T_R} \right) \quad (5.1)$$

where  $k(T)$  is the rate constant at temperature  $T$ ,  $k(T_R)$  is the rate constant at the reference temperature,  $Q$  is the activation energy, and  $R$  is the universal gas constant. By plotting  $\Delta$  versus  $T^{-1}$ , the activation energy is obtained through the slope of the curve [Lachter et al., 1986]. As shown in Figure 5.8, the obtained activation energy is  $102 \pm 6$  kcal / mol.

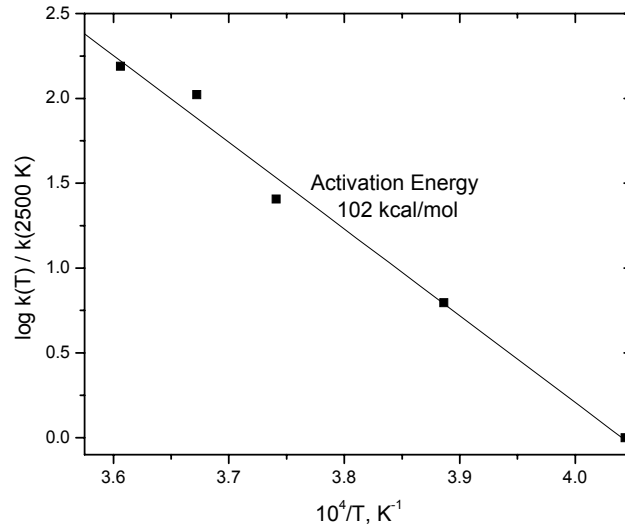


Figure 5.8: Ratio of rate constants versus  $T^{-1}$

It has been concluded from extensive study of other carbon systems that graphitization occurs by a progressive, homogeneous improvement of the disordered structure [Pacault, 1971]. This is believed to occur by one common, thermally activated rate-controlling mechanism that has a single, well-defined activation energy independent of temperature and of the degree of structural perfection. The mechanism which is considered most likely is mass-transport via self-diffusion by one or more point defect

mechanisms, and the activation energy for this is  $\sim 240$  kcal/mol. However, the effect of preferred orientation, while generally agreed to be important in determining graphitizability, remains largely unknown and may be complex [Fishbach, 1971].

In this light, the lower value of the activation energy for the graphitization of MCMB determined above may be appropriate. The generally accepted structure of MCMB includes layers of molecules that are well defined prior to any additional heat-treatment. This structure arises from the liquid-crystal mesophase formation within the parent pitch and persists through carbonization to graphitization [Hu et al., 2004]. It appears that this ordered arrangement of MCMB results in lowering the activation energy. The influence of precursor carbon structure on graphitization has also been noted previously [Franklin, 1951].

There are several other factors which could also lead to a lower effective energy, even assuming that self-diffusion by a defect mechanism is the dominant process. Reduced defect formation energies, “short-circuit” diffusion paths, and excess concentrations of defects in the disordered structure would all lead to decreases in activation energy. However, there is no evidence that MCMB includes any of these features, and therefore this data indicates the effect of preferred orientation on graphitization kinetics. This may also suggest that the theory graphitization occurs by one process with a single, well-defined activation energy value does not capture all the subtleties involved in the actual process [Pacault, 1971].

#### **5.4 Conclusion**

The high temperature sintering behavior of MCMB has been investigated. The observed shrinkage is accompanied by similar increases in pycnometric density, which result in constant, rather than decreased, porosity content. However, observed changes in pore microstructure indicate that a high-temperature sintering mechanism may be active which could result in overall porosity elimination. This mechanism likely progresses slowly, and sintering times which may result in fully dense samples are outside the scope of this work. Thus, while the low temperature sintering behavior of MCMB is unique, the high temperature sintering appears to be similar to that of conventional materials.

For the graphitization kinetics of MCMB, an activation energy of  $\sim 100$  kcal/mol was obtained. This is lower than the value for many other types of carbon (240 kcal/mol) and indicates the effect of preferred orientation on graphitization kinetics, which is largely unknown and may be complex. Further, the graphitization of MCMB may lead to greater fracture resistance of individual microbeads, and additional studies in this direction are required.

In summary, the combination of excellent compressibility (up to 94% relative density), unique low temperature sinterability, and rapid graphitization make mesocarbon microbeads an attractive precursor for manufacturing carbon-based materials.

## CHAPTER 6

### REACTION BONDING BY IN-SITU SILICON CARBIDE AND NITRIDE FORMATION

The discussion presented in Chapter 2 leads to the idea that reinforcement may be an effective method for increasing the fracture toughness of materials based on mesocarbon microbeads. However, there are novel methods of introducing reinforcements that may prove to increase the mechanical properties beyond more conventional approaches. One possibility is to introduce precursors and allow reactions during heat treating to form reinforcement phases *in-situ*. For example, Si added to MCMB will react to form SiC during heat treatment. It is possible that the chemical bonds formed between Si and MCMB will increase the strength of interparticle bonds, thereby improving the fracture toughness of the sample. This chapter is focused on processing in-situ reinforced composites using silicon.

#### **6.1    *Experimental Methods***

Investigation of one type of commercially available mesocarbon microbeads (Osaka Gas, Japan), whose characteristics are summarized in Table 3.1, is continued.

This chapter reports on the in-situ formation of reinforcement silicon carbide and nitride. This was studied in two ways. Silicon particles were added to MCMB by the liquid mixing procedure described in section 3.1.1. Also, a Si-containing polymeric precursor was added to the MCMB as detailed in section 3.1.4. These samples were then compacted at pressures about 400 MPa with a dwelling time of 3 minutes, as reported in Chapter 3. For MCMB-Si mixtures, increasing Si volume fraction decreases the green relative sample density (pure MCMB,  $\rho=0.95$ ; 20 vol% Si in MCMB,  $\rho=0.85$ ). This effect owes to the lower compressibility of Si powder as compared to the MCMB. The behavior during sintering was studied using dilatometry (see Chapter 3). Experiments were conducted with a flowing atmosphere of either high purity nitrogen or argon.

Thermogravimetric analysis (TGA) was performed to study the reaction kinetics in the nitrogen / Si / MCMB system. To define product phase composition, x-ray diffraction (XRD) patterns were collected. Finally, sample microstructures were investigated. The details of these procedures are described in Chapter 3.

## **6.2 Results**

### **6.2.1 Reactions in Argon**

Detailed investigations into the shrinkage behavior of the Si-MCMB system were accomplished using dilatometry. In addition to measuring the dimensionless shrinkage  $\lambda = (L - L_0)/L_0$  (where  $L$  is the sample length and  $L_0$  is the initial sample length), additional insight into the sintering process was gained by calculating the shrinkage rate,  $d\lambda/dT$ . Figure 6.1 shows the typical dilatometric results for samples containing 20 vol% Si when

heat-treated at  $W = 1\text{ }^{\circ}\text{C}/\text{min}$  to  $1500\text{ }^{\circ}\text{C}$  in an argon atmosphere (curves 1 & 2). The low temperature behavior was similar to the swelling observed for pure MCMB (curves 3 & 4, see also Chapter 4). The maximum in shrinkage rate, which occurs at  $\sim 725\text{ }^{\circ}\text{C}$ , was only slightly less intense for the sample containing Si. Further, there was a sudden swelling event observed at  $\sim 1375\text{ }^{\circ}\text{C}$ , after which the shrinkage rate quickly approached zero. It was also verified by XRD that Si completely converts to  $\beta\text{-SiC}$  for composites containing up to 20 vol% Si when heat treated by this method. In addition, it was noted that detectable SiC was formed after heat treatment to  $1350\text{ }^{\circ}\text{C}$ , which is below the melting point of Si ( $1414\text{ }^{\circ}\text{C}$ ). Thus the Si-C reaction initiated while Si was in the solid state.

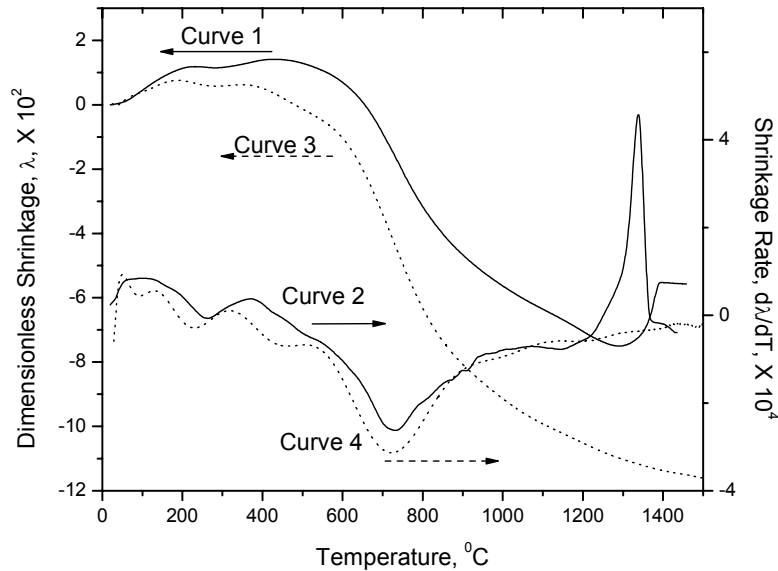


Figure 6.1: Comparison of typical dilatometric results. ---- (curves 3 and 4): pure MCMB, —(curves 1 and 2): 20 vol.% Si in MCMB;  $W=1\text{ }^{\circ}\text{C}/\text{min}$  in argon

In an attempt to investigate the effect of the time-temperature schedule on the swelling event observed above 1300 °C, experiments were conducted with the program altered to include pretreatment at various temperatures for different durations prior to heating above the melting point of Si, i.e., to 1500 °C. Isothermal soaks of 12 – 24 hours were programmed into the time-temperature schedule. Including these holds resulted in changing the swelling peak position and intensity, but did not increase the overall shrinkage obtained. However, when the time temperature schedule was altered to have an extremely low heating rate of  $W = 0.1$  °C/min, the observed swelling event was reduced and shrinkage increased (Figure 6.2).

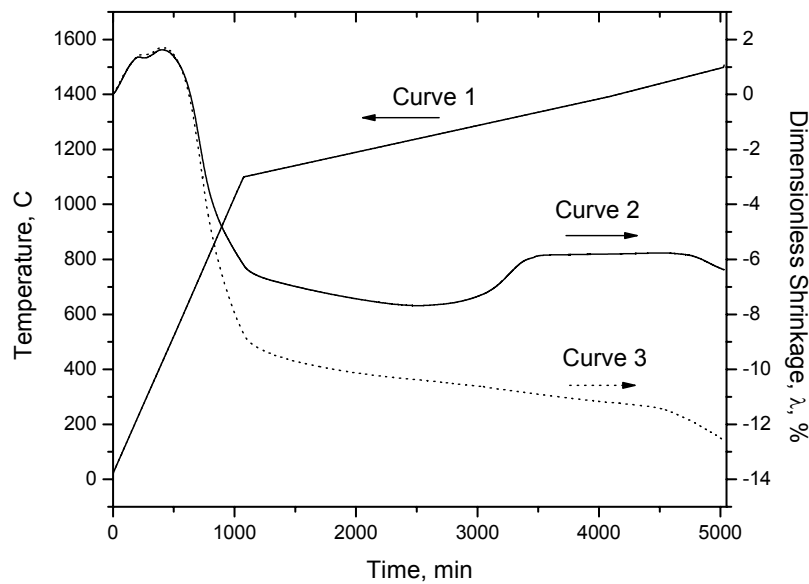


Figure 6.2: Dilatometric results with extremely low heating rate of  $W = 0.1$  °C/min in range 1100 – 1500 °C. Curve 1 represents the temperature and Curves 2 & 3 the shrinkage of composite systems of 20 and 5 % Si in MCMB, respectively

Figures 6.3 a and b show the typical microstructure for samples heat-treated at  $W = 1\text{ }^{\circ}\text{C}/\text{min}$  to  $1500\text{ }^{\circ}\text{C}$ . As confirmed by EDS, the large, dark particles are MCMB, and the fine phase between the beads is SiC. This is compared with the microstructure of a sample heat treated to  $800\text{ }^{\circ}\text{C}$  in Figure 6.3 c. As heat treatment to  $800\text{ }^{\circ}\text{C}$  is insufficient to induce any SiC formation, this microstructure can be used to determine the changes in morphology during reaction. The distinguishing characteristic of the final microstructure is the porous appearance of the SiC phase, not observed in the unreacted microstructure. One possible explanation for the development of this porosity is that the formation of SiC decreases the volume of the system, due to the higher density of the product ( $3.22\text{ g}/\text{cm}^3$ ) over the reactants ( $\text{Si} = 2.33\text{ g}/\text{cm}^3$ ,  $\text{MCMB} = 1.99\text{ g}/\text{cm}^3$ ). It can easily be shown that this volume decrease should be on the order of 31%. The scale of homogeneity is also drastically decreased by this reaction. The final microstructure has fine nanoscale pores, along with a fine SiC network (Figure 6.3 b).

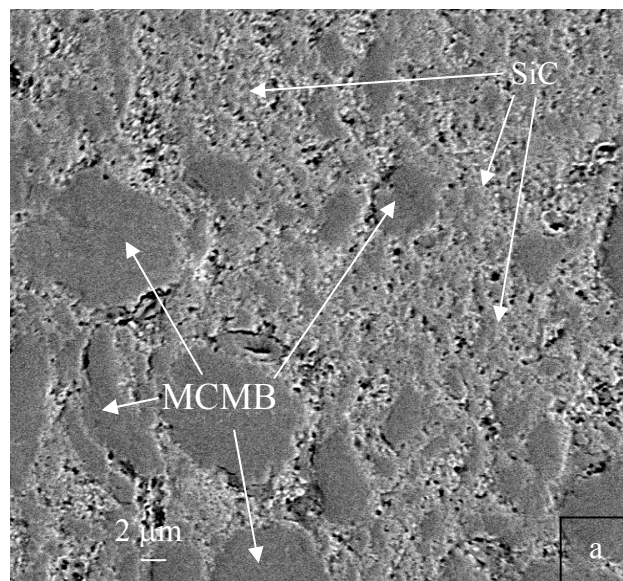


Figure 6.3 a: Typical microstructure for 20 vol% Si in MCMB heat treated  $W=1\text{ }^{\circ}\text{C}/\text{min}$  in argon to  $1500\text{ }^{\circ}\text{C}$ , low magnification



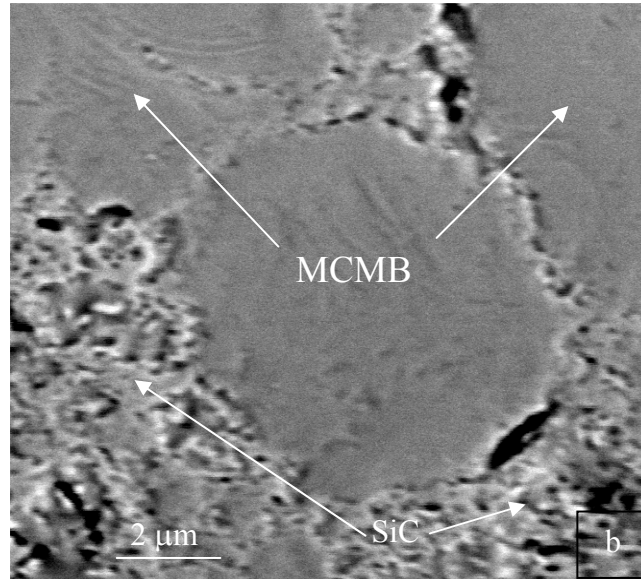


Figure 6.3 b: Typical microstructures for 20 vol% Si in MCMB heat treated  $W=1$  °C/min in argon to 1500 °C, high magnification

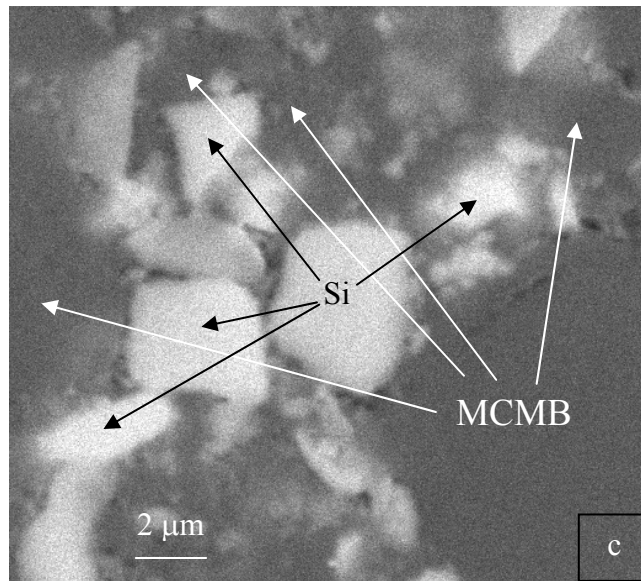


Figure 6.3 c: Typical microstructure for 20 vol% Si in MCMB heat treated  $W=1$  °C/min in argon to 800 °C.

### 6.2.2 Reactions in Nitrogen

Figure 6.4 shows the typical dilatometric results for samples containing 20 vol% Si when heat-treated at  $W = 1\text{ }^{\circ}\text{C}/\text{min}$  to  $1500\text{ }^{\circ}\text{C}$  in a nitrogen atmosphere (curves 1 & 2). As for the reactions in argon, the low temperature swelling behavior was largely the same as of pure MCMB (curves 3 & 4), and the maximum in shrinkage rate was slightly tempered by the presence of Si. A sudden swelling event centered at  $\sim 1425\text{ }^{\circ}\text{C}$  was observed, although it was less intense than in argon (compare with Figure 6.1). This swelling event also affected the overall shrinkage achieved by the sample.

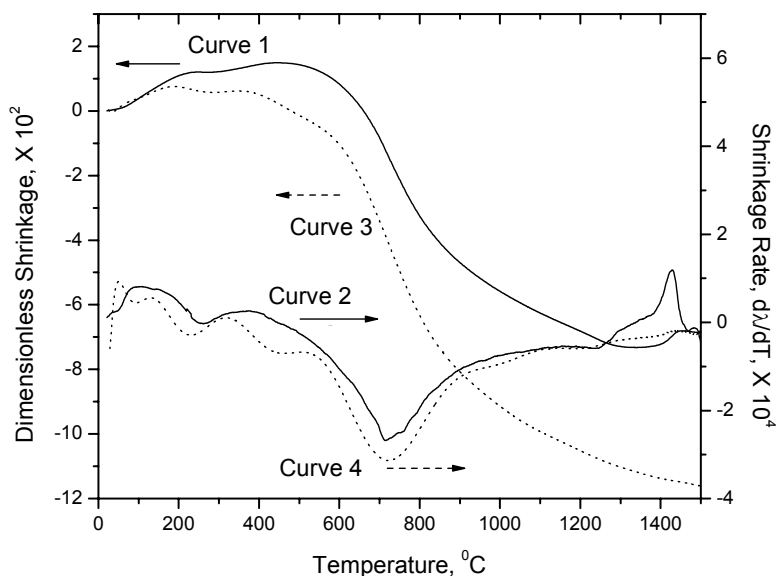


Figure 6.4: Comparison of typical dilatometric results. ---- (curves 3 and 4): pure MCMB, —(curves 1 and 2): 20 vol.% Si in MCMB;  $W=1\text{ }^{\circ}\text{C}/\text{min}$  in nitrogen

To determine if the observed swelling event could be avoided, the time-temperature schedule was altered to include a 12 hour hold at 1350 °C prior to heating to 1500 °C. This changed the composition of the obtained composite, which was monitored via XRD. It was determined that the isothermal hold increased the amount of silicon nitride formed relative to the amount of carbide formed. Further, the swelling event observed via dilatometry was eliminated, and the overall sample shrinkage increased, as shown in Figure 6.5.

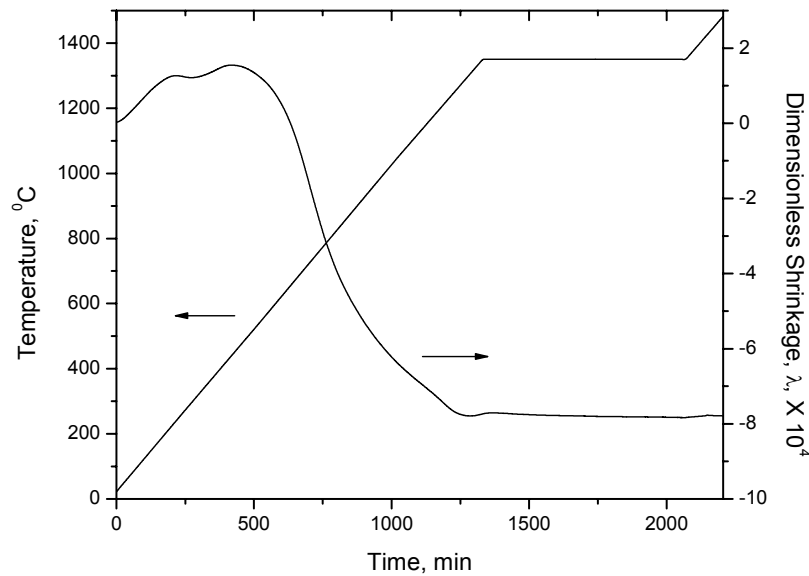


Figure 6.5: Dilatometric results for 20 vol.% Si in MCMB processed in nitrogen

The system's reaction with nitrogen was studied using TGA. Figure 6.6 compares the change of mass during heating to 1500 °C for the following two compositions: MCMB with 28 wt% SiC (curve 1) and MCMB with 28 wt% Si (curve 2). It is assumed that the system containing SiC did not react with nitrogen, and therefore represents the amount of mass which would be lost by the system in an inert atmosphere owing to expected evolution of gaseous products associated with heating MCMB. On the other

hand, the system containing Si began to react with nitrogen at  $\sim 1000$  °C. The conversion of Si to  $\text{Si}_3\text{N}_4$  can be estimated from the amount of nitrogen adsorbed from the atmosphere (curve 3). It was seen that the reaction begins at about 1000 °C; in contrast, no reaction to form SiC can be detected after heat treatment to this temperature. Also, it was observed that significant conversion was achieved by preheating to 1350 °C.

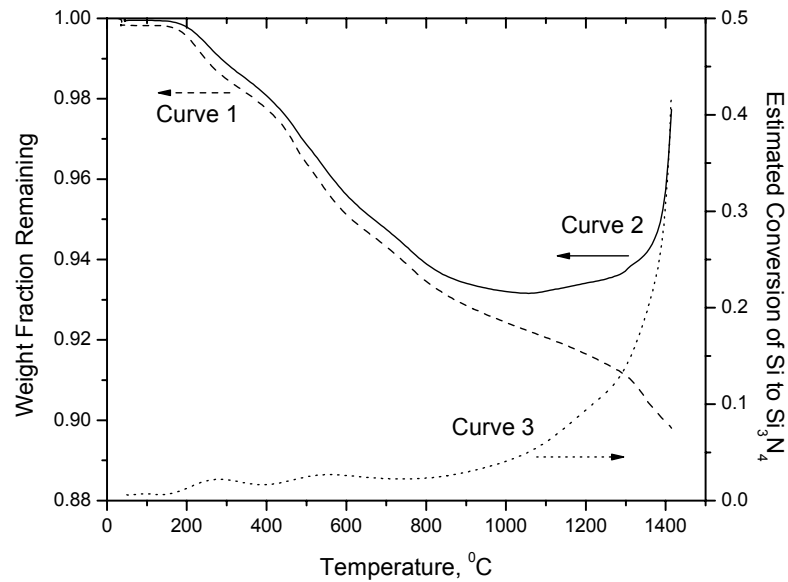


Figure 6.6: Results of TGA on 28 wt.% SiC in MCMB (Curve 1) and 28 wt.% (20 vol.%) Si in MCMB (Curve 2) processed in nitrogen. Curve 3 shows the estimated conversion of Si to  $\text{Si}_3\text{N}_4$  based on the uptake of nitrogen

Figure 6.7 shows the typical microstructure for samples containing 20 vol% Si in MCMB heat treated at 1 °C/min to 1500 °C in nitrogen. EDS analysis reconfirmed that the large, dark particles were the microbeads, while the light phase represented both SiC and  $\text{Si}_3\text{N}_4$ . The distinguishing characteristic of this morphology was the close association between the reacted SiC/  $\text{Si}_3\text{N}_4$  and the carbon beads. It was observed that there were carbon phases imbedded in regions of SiC/  $\text{Si}_3\text{N}_4$ . Also, the contact between carbon and SiC/  $\text{Si}_3\text{N}_4$  particles was intimate in many cases. Note also, in contrast to that seen in

Figure 6.3, there was little appearance of porosity in the SiC/ Si<sub>3</sub>N<sub>4</sub> phase. It appears that the volume decrease owing to SiC formation described above is, in part, counteracted by the volume increase when Si reacts to form Si<sub>3</sub>N<sub>4</sub> (~13%).

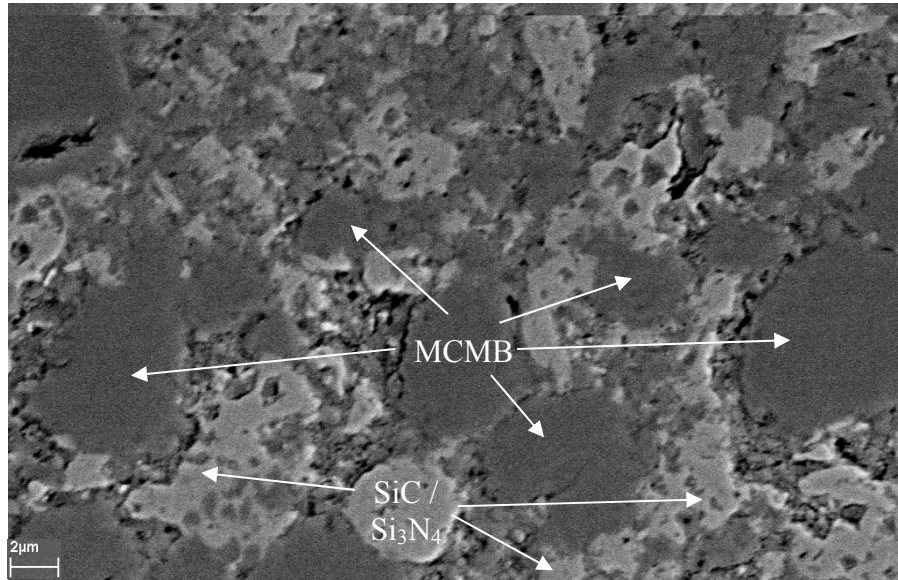


Figure 6.7: Typical microstructure for 20 vol.% Si in MCMB heat treated W=1 °C/min to 1500 °C in nitrogen

### 6.2.3 Polymeric Decomposition

Figure 6.8 shows the dilatometric results for a system which contained enough PCS to give 5 vol% SiC in the final composite when heat treated at 1 °C/min to 1500 °C in an argon atmosphere. Owing to a greater maximum rate, the sample shrinkage (~13%) was enhanced versus that for the pure MCMB (~11.5%). Also, note the absence of any high-temperature swelling event. This is an encouraging result, as the decreased shrinkage in composite systems is a significant hurdle that prevents MCMB from forming fully dense composites.

Additional samples were processed in a nitrogen atmosphere. This change in the experimental conditions had no detectable effect on the final dimension changes, mass loss, or sample morphology; furthermore, no nitride formation was detected by XRD.

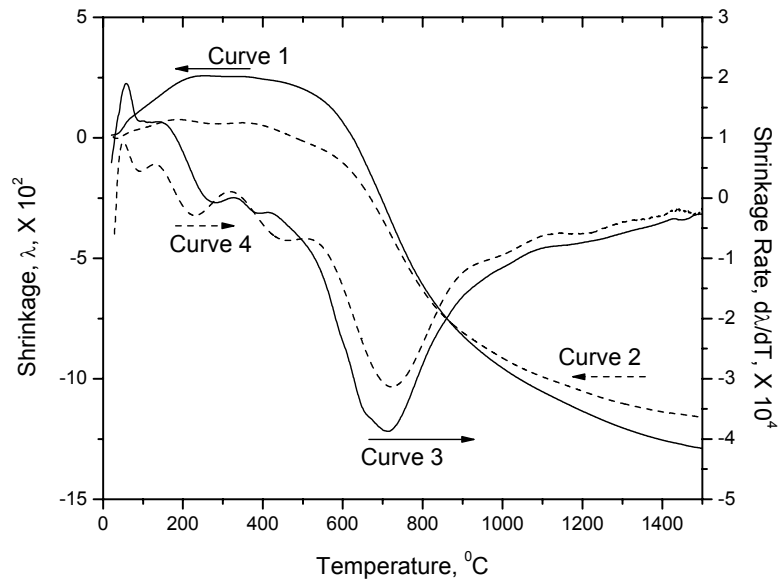


Figure 6.8: Comparison of typical dilatometric results. ---- (curve 2 and 4): pure MCMB, —(curve 1 and 3): PCS-MCMB; W=1 °C/min in argon

Figure 9 shows the typical microstructure for these samples. Note the close association between carbon particles that may indicate that the decomposition of the polymer does not interfere with the shrinkage expected for the carbon. This micrograph clearly showed the new phase created, which appeared as a thin, uniform coating of SiC on the MCMB surface.

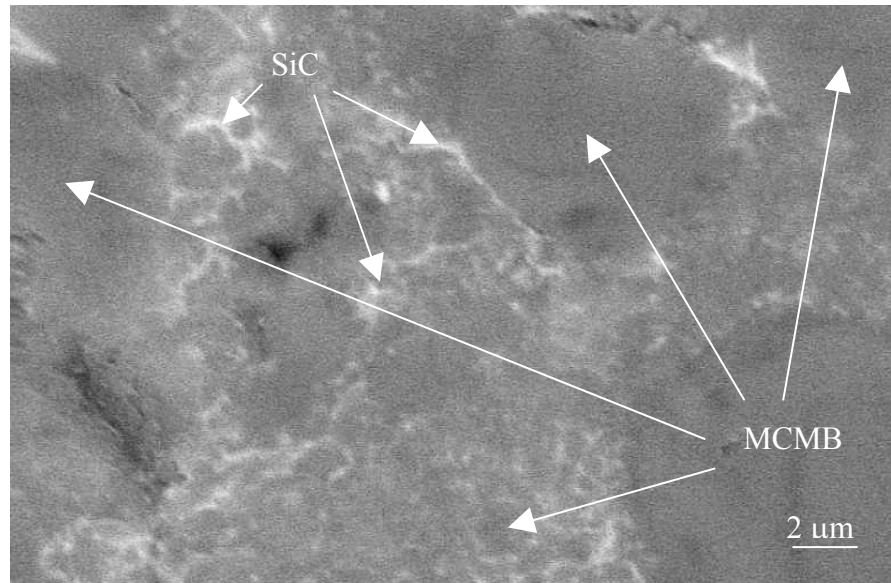


Figure 6.9: Typical microstructure for PCS-MCMB

### 6.3 Discussion

The discussion begins with examination of the high-temperature swelling event observed via dilatometry. Then the formation of reinforcements by polymeric decomposition is discussed, and finally recommendations are made for further work in this area.

#### 6.3.1 High-Temperature Swelling in Silicon / MCMB Composites

As observed above, there was an unusual swelling event centered at  $\sim 1375$  °C when samples containing 20 vol% Si are processed at  $W = 1$  °C/min in argon (see Figure 6.1). Also, it was shown that varying the heating schedule to include isothermal holds alters the temperature and intensity of the swelling event. From this, it was concluded

that the swelling temperature is not a characteristic of the system. Additionally, when the heating rate was very slow (Figure 6.2), the swelling event was greatly reduced.

A similar swelling event was observed when the same samples were processed in nitrogen (Figure 6.4). However, it achieved a maximum above the melting point of Si. It can be concluded that this swelling was due to the formation of liquid Si, which resulted in liquid penetration between the grains [German, 1996; Li and Hausner, 1996]. Note that while the swelling in this system initiated at temperatures similar to those observed in argon (Figure 6.1), the maximum swelling rate was delayed to higher temperatures. Thus the swelling mechanism active in argon was also present in nitrogen, but to a lesser extent.

It was suggested that the earlier swelling was associated with the direct interaction of Si and MCMB, which may be retarded by the formation of  $\text{Si}_3\text{N}_4$ . As shown in Figure 6.6, significant conversion of Si to  $\text{Si}_3\text{N}_4$  was possible at relatively low temperatures (prior to significant SiC formation). Previous research indicated that  $\text{Si}_3\text{N}_4$  layers are formed on the surface of Si particles at temperatures below the melting point of silicon [Pigeon et al., 1993]. This resulted in a  $\text{Si}_3\text{N}_4$  barrier, which prevented the direct interaction of pure Si and MCMB, avoiding additional swelling. Upon reaching the melting point of pure Si, the  $\text{Si}_3\text{N}_4$  shell cracked and liquid Si escaped. The formation of liquid Si was avoided by prolonged heat treatment below the melting point of Si, which allowed for greater conversion of Si to both  $\text{Si}_3\text{N}_4$  and SiC, leaving little or no material available for liquid formation. This eliminated the observed swelling event (see Figure 6.5) and led to increased shrinkage ( $\lambda=-7.7$  when held at 1350 °C for 12 hours) as compared to an uninterrupted heating rate ( $\lambda=-6.8$ , see Figure 6.4).



The swelling caused by the direct interaction of Si and MCMB was believed to also be due to the melting of Si. Melting can occur when the external temperature was below the melting point of Si due to the exothermic reaction between Si and carbon to form SiC. This reaction produced sufficient energy to melt unreacted Si, which was observed as swelling. Thermodynamic estimates showed that the temperature can be significantly higher (up to 400 °C) than the external temperature under adiabatic conditions. This explanation is consistent with the observation that lower heating rates resulted in the observation of swelling at lower temperatures; essentially, higher heating rates allowed the external temperature to increase while the actual sample temperature was elevated by the energy released by the reaction. This explanation was also supported by the results shown in Figure 6.2; the low-heating rate allowed for reaction between Si and MCMB to progress gradually, which led to small amounts of energy being produced slowly. This allowed for reduction in the amount of swelling observed and an increase in overall shrinkage ( $\lambda = -5.6$  when  $W = 1$  °C;  $\lambda = -6.4$  when  $W = 0.1$  °C).

Additionally, it was observed in Figure 6.2 that at very long times ( $t > 4750$  min), an additional shrinkage mechanism becomes active. This was believed to be caused by sintering of the reinforcement phases. Thus, through careful processing, further sintering was achieved, which reduces the overall porosity of the composite. Note also that the system containing 5 vol% Si in MCMB achieved overall shrinkage on the order of 12.5% (curve 3), which is greater than that achieved by pure MCMB (~11.5%). Thus it was concluded that the suggested approach, i.e., careful control of reaction bonding conditions and the sintering of reinforcements, is promising for the production of low porosity carbon composites.

### 6.3.2 *Polymeric Decomposition*

As seen in Figure 6.8, the dilatometric results for the PCS / MCMB system showed enhanced shrinkage characteristics over the pure MCMB system. In contrast to the effect of other reinforcement phases, which generally disrupt the particle-to-particle contact needed for sample shrinkage (see Chapter 4), the presence of the PCS in the system allowed for maintained contact. The enhancement was due to a more intense maximum in the shrinkage rate and resulted from decomposition of the polymer. The polymer either evolved some mass, or increased its density, both resulting in additional shrinkage. Literature on the subject indicated that the polymer may undergo condensation reactions, both with the MCMB and within the polymer chain, resulting in only small mass losses [Czosnek et al., 2002]. It was therefore expected that these reactions result in increasing density of the products over the initial polymer, leading to shrinkage.

The used mixing procedure resulted in a uniform, thin coating of polymer on the MCMB surface, which in turn led to uniform SiC layer formation after heat treatment (Figure 6.9). Note that SiC layers appeared to be nanosized (~100 nm). The absence of high temperature swelling effects and a uniform distribution of tough nanoparticles along the surface of the carbon phase were encouraging results. Since this polymer also enhanced the shrinkage characteristics (Figure 6.8) of the MCMB-based composites, it was concluded that the suggested approach, i.e., nanoscale reinforcement of carbon-based composites, using low melting polymeric compositions, is attractive.

#### **6.4 Conclusion**

The ultimate goal of this work is to advance the technology required for the rapid, low-cost processing of MCMB to carbon-based high performance materials. In the results discussed above, we gained several important insights into the use of reinforcements in this system: (i) exothermic reactions can lead to undesired swelling events when using reaction bonding; (ii) through careful processing, additional sintering of the reinforcement phase can be achieved, reducing the composite porosity; (iii) formation of nanoscale reinforcements through decomposition of silicon containing polymers increased the shrinkage rate, leading to enhanced overall sample shrinkage; and finally, (iv) it is possible to control the microstructure, composition, and shrinkage of the silicon-MCMB system by manipulating the processing conditions, i.e., the time-temperature schedule and the processing atmosphere.

## CHAPTER 7

### MECHANICAL PROPERTIES OF MCMB-BASED MATERIALS

Chapter 6 describes some issues which may be encountered in processing MCMB-based composite systems, especially when in-situ reinforcement is used. This chapter will explore the effect of in-situ reinforcement and compare its effects to reinforcement without reaction, i.e., the addition of refractory carbides. This will be studied via mechanical tests, specifically hardness and fracture toughness, and will be compared to the properties of pure MCMB samples. 0

#### **7.1 *Experimental Methods***

Both composite and pure MCMB systems were investigated. Tungsten (W) and tungsten carbide (WC) were introduced via milling. The W/WC system was chosen as a convenient illustration of in-situ reinforcement formation, but many other systems exhibit this phenomenon, including silicon, titanium, boron, and zirconium, to name a few.

The MCMB were calcined prior to use as described in Chapter 3. The powders were uniaxially pressed in a 31 mm cylindrical die at pressures about 300 MPa with a dwelling time of 9 minutes. Several samples of pure MCMB were compacted at about 60 MPa, resulting in lower relative green density, to determine the effect of porosity on

fracture toughness. Samples were heat treated in the graphite resistance furnace, at 1 °C/min to 1500 °C, then 25 °C/min to 2450 °C for a 5-hour soak. These were machined by electron discharge and compact tension testing was performed. Fracture surfaces were investigated using a scanning electron microscope. Hardness was measured via superficial Rockwell measurements.

Preliminary measurements were made on samples which were polished to a mirror finish. This treatment did not influence the obtained mechanical properties, and thus all data reported are for unpolished samples.

## **7.2 *Results and Discussion***

### **7.2.1 *Fracture Toughness***

Samples were prepared with varying amounts of W and WC. It was confirmed by XRD that W is fully converted to WC during heating. As the makeup of the reinforcement phase changes due to reaction, compositions were carefully controlled to yield a known volume percent of the product (WC) in the final composite. The formation of reinforcements in-situ may lead to increases in mechanical properties, as discussed in Chapter 6. Figure 7.1 shows the dependence of fracture toughness on reinforcement content. While reinforcement does not increase fracture toughness, the mechanical properties of the composite systems are not greatly reduced from that of the pure MCMB. This is similar to previous research, which has shown that the addition of carbides does not strongly influence the mechanical properties of pure graphite. The values shown

agree reasonably well with other investigations into similar systems [Garcia-Rosales et al., 2002].

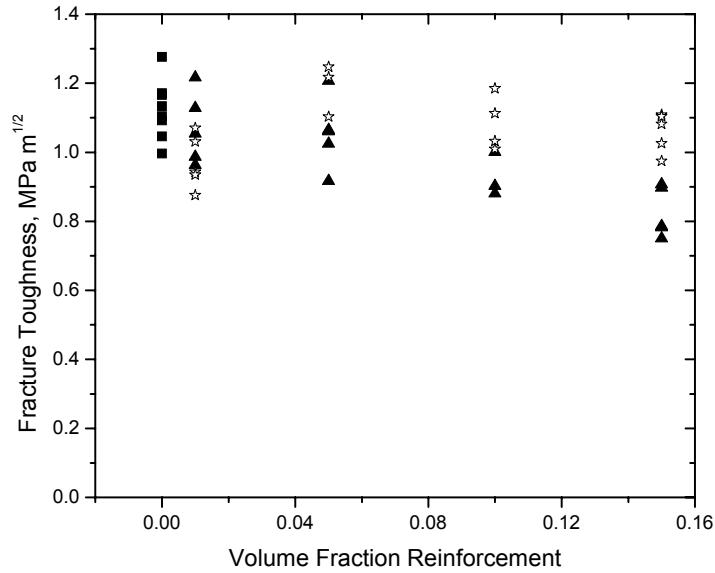


Figure 7.1: Dependence of fracture toughness on volume fraction of different reinforcement phases: ■ - pure MCMB, ▲ - W addition, ☆ - WC addition

The data displayed above do not allow delineation between two competing effects. As described in Chapters 3 and 6, the relative green density of composite systems decreases due to the lower compressibility of the reinforcement phases. Additionally, it is expected that the relative density of the samples remains largely constant. This means that the porosity of the composite samples will be higher than that of pure samples. Porosity is well known to have deleterious effect on mechanical properties [Callister, 1997]. We therefore gain additional insight by examining the fracture toughness as a function of density (Figure 7.2). The relationship between relative density and fracture toughness has several features which must be noted. First, this treatment does not affect the most important conclusion, that the desired increase in

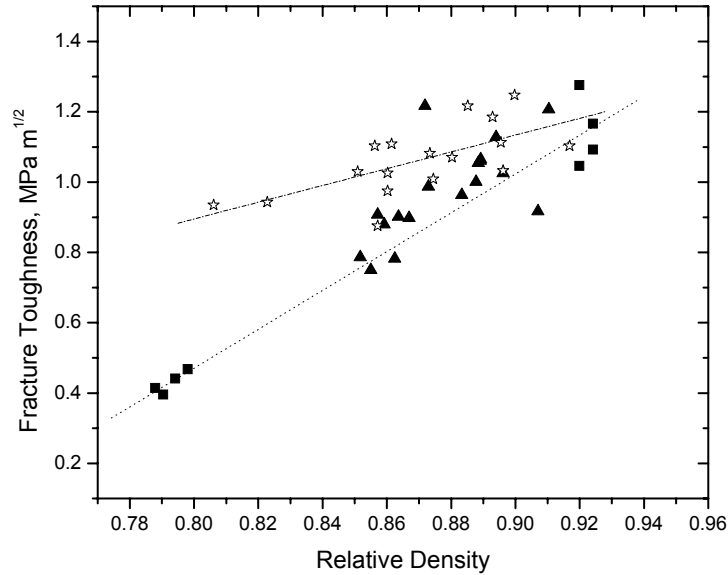


Figure 7.2: Dependence of fracture toughness on density for several different reinforcement types and amounts: ■ - pure MCMB, ▲ - W addition, ☆ - WC addition

fracture toughness was not realized by the inclusion of reinforcements. Second, that the slope of the line for pure MCMB samples is larger than that for samples with WC added. This indicates that composites containing WC are more tolerant of porosity than samples made of pure MCMB. Therefore, it is concluded that reinforcement is having some positive effect on the mechanical properties. Finally, it should be noted that the data collected for in-situ formation of WC (resulting from W addition) fall generally above the line for the pure MCMB samples. This indicates that in-situ reinforcement formation also increases the mechanical properties, although not to the same extent as addition of WC. Increases in mechanical properties may be caused by reinforcement mechanisms discussed in Chapter 2, and may also be attributed to changes in the pore microstructure which accompany processing carbon reinforced with carbides.

### 7.2.2 *Fractography*

Analysis of the fracture surface shown in Figure 7.3 was performed using SEM. The fracture surface for pure MCMB samples (Figure 7.3 a) indicates that the fracture mode is largely intergranular. Areas can be identified where beads appear to have been removed from the surface, and no fractured grains can be identified. This fracture mode occurs when bonding between grains is weak in comparison with the strength of the grains. However, examining the fracture surface for a typical composite (15 vol% W addition) shows that the fracture mode has changed to a mixture of intergranular and transgranular fracture. Transgranular fracture leaves behind markings which can easily be observed (for example, see Figure 7.3 c). This type of fracture is favored when bonding between grains is strong in comparison with the strength of the grains. This mixed mode of fracture indicates that compositing has succeeded in strengthening the bonding between grains [Varner, 1991].

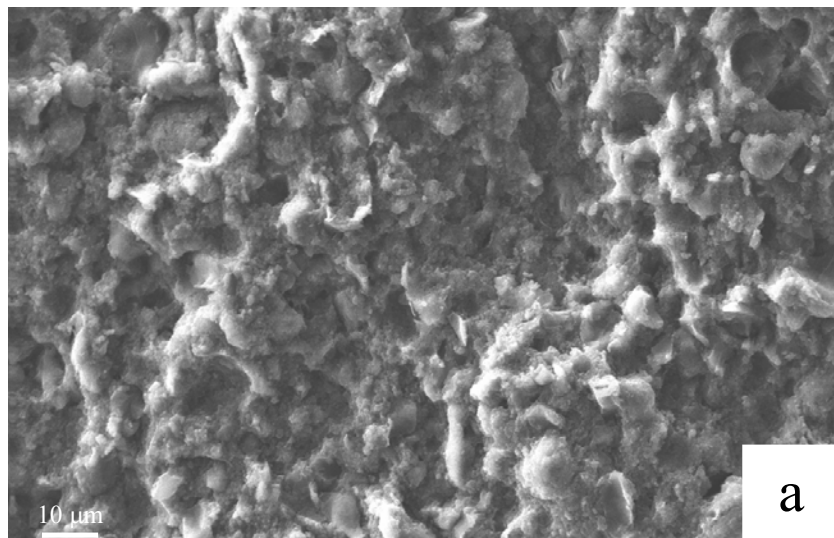


Figure 7.3 a: Fracture surface of pure MCMB sample



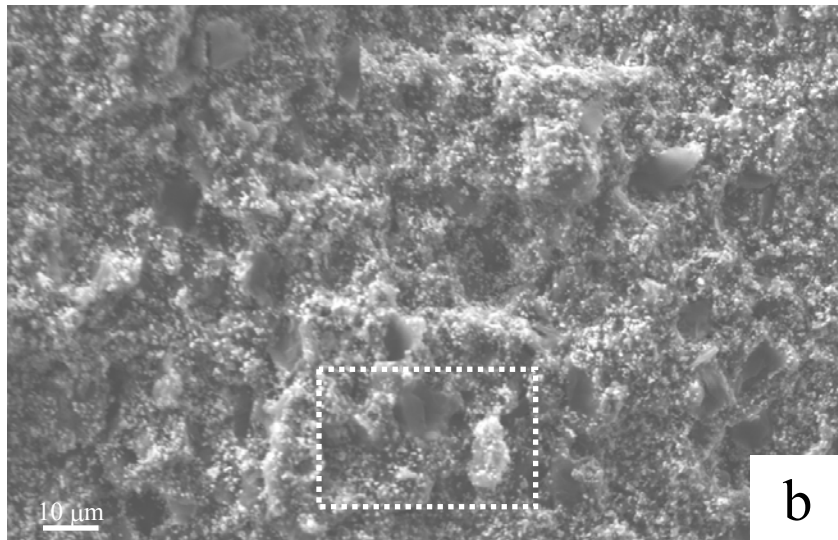


Figure 7.3 b: Fracture surface of sample with 15 vol% tungsten

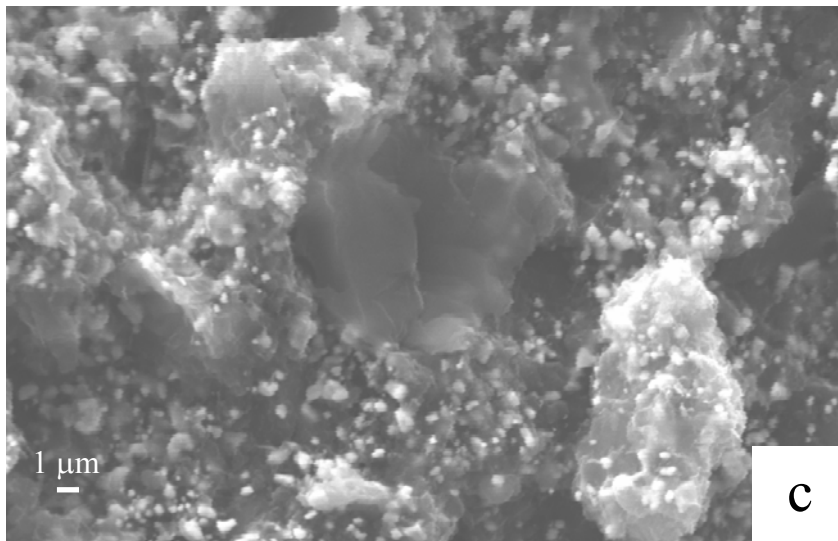


Figure 7.3 c: An expanded view of the fracture surface area shown in 7.3 b

### **7.2.3 Hardness**

Superficial Rockwell results are presented in Table 7.1, where each entry is the average of 25 measurements on the same sample. Similar to what was observed above, the hardness of pure samples is superior to that of all composite systems. Addition of as little as 1 vol% results in 5 – 25% reduction of hardness, as measured at 15 kg loading. Similar decreases were observed when the major load of indentation was 30 kg. Further, it was shown that for samples containing 20 vol% of all studied reinforcements, the hardness test did not yield meaningful results. This was either due to a complete fracture of the sample, invalidating the test, or penetration greater than the height of the indenter used (1/16 inch spherical indenter), resulting in contact between the testing fixture and the sample.

These findings are consistent with the observations made concerning compact tension testing. It is likely that the decrease in hardness is largely due to increased porosity that is concomitant with the addition of reinforcement phases.

## **7.3 Conclusion**

It was observed that the mechanical properties decrease with the addition of reinforcing phases. However, it was also shown that reinforcement may in fact increase the mechanical properties as compared to those of pure MCMB at the same porosity content. This indicates that a major hurdle to increasing the mechanical properties of MCMB-based materials is the introduction of reinforcement phases while maintaining high (~95%) relative density. Some work described in Chapter 6, especially that on polymeric decomposition, relates to this problem. This relationship is further

TABLE 7.1

SUPERFICIAL ROCKWELL HARDNESS RESULTS FOR VARIOUS MCMB  
SAMPLES

Reinforcement	Reinforcement content, vol %	Load, kg	Hardness
Pure	0	15	85 85 87
Si	1 %	15	79 74
SiC	1%	15	78 79
Ti	1%	15	67 65
TiC	1%	15	75 72
TiN	1%	15	73 79
Pure	0	30	71 61
Si	1%	30	51
SiC	1%	30	52
TiC	1%	30	52
TiN	1%	30	54
Si	20%	15	Neg
Si	20%	30	Neg
SiC	20%	15	Neg
SiC	20%	30	Neg
TiC	20%	15	29
TiC	20%	30	Neg
Ti	20%	15	43
Ti	20%	30	Neg

complicated by the catalytic effect that many reinforcement materials, such as carbides, have on graphitization [Garcia-Rosales et al., 2002]. As mentioned in Chapter 5, graphitization may be related to mechanical properties, as in carbon fibers.

As described in Chapter 3, the ASTM standard used was not designed specifically for brittle materials. Consequently, there may be difficulties in implementing it for testing MCMB-based materials. Specifically, the standard requires an atomically sharp crack be fatigued into the sample prior to tension testing. This was attempted with pure MCMB samples, however, suitable fatigue conditions were not found. It is therefore suggested that the obtained results may not be precise in the determination of fracture toughness. This data is still believed to be valuable in identifying the described trends, however, a more suitable test, such as chevron-notch or three point bending, is recommended for future evaluation.

## CHAPTER 8

### CONCLUSION

In Chapter 2, a number of areas requiring investigation were identified. In this brief chapter, progress in these matters is reiterated, and directions for further work are identified.

#### **8.1    *Summary of Work***

The relationship between shrinkage and evolution of density was delineated in Chapter 4. It was shown that during heat treatment, necks formed between particles as a result of a non-densifying *liquid-phase sintering mechanism*, which was active at temperatures  $< 800$  K. Further, sample shrinkage was attributed solely to *changes in true particle density* resulting from crystallographic rearrangement, observed in the region 800 – 1200 K.

Further, it was determined that the high temperature (1900-2800 K) sintering of MCMB is similar to that of *conventional carbon-based materials*, and the mechanisms which result in overall porosity elimination are slow (see Chapter 5). In contrast, the obtained activation energy for high-temperature graphitization (100 kcal/mol) is less than half the value for typical carbon (240 kcal/mol). This is indicative of the effect of

preferred orientation on the process, which is largely unknown and may be complex. It is also suggested that the performance of MCMB-based materials may be dependent on graphitization.

One problem, namely *swelling* caused by melting of precursors due to exothermic reactions during in-situ reinforcement formation, was discussed in Chapter 6 as it relates to the Si system. It was seen that through careful processing these undesired events can be minimized or avoided. These techniques include slow heat-treatment and the use of different reaction atmospheres (such as nitrogen) to reduce exothermicity.

It was also observed that during very long sintering times, the sintering of the *reinforcement phase* contributes to the overall shrinkage of the composite. Further, the formation of *nanosized reinforcements* was achieved through *polymeric decomposition*. Both sintering of reinforcement phases and in-situ reinforcement via polymeric precursors were shown to increase the shrinkage of the composite system, decreasing total porosity. Both of these directions are promising for further research.

The mechanical properties of MCMB-based materials were studied and reported in Chapter 7. It was seen that reinforcement made samples *more tolerant* to porosity, and that inclusion of reinforcements increased the bonding strength between grains.

Based on these studies, it is clear that the combination of *excellent compressibility* (up to 94% relative density), *unique low temperature sinterability*, and *rapid graphitization* make mesocarbon microbeads an attractive material for manufacturing carbon-based materials.

## 8.2 *Suggested Areas for Future Research*

Based upon the above conclusions, several areas for additional research can be identified.

From the results of Chapters 4 and 5, it was seen that bonding between the microbeads is introduced from the action of the  $\beta$ -resin, which is active  $<800$  K (Chapter 4). Further bonding between the grains may be accomplished through solid state sintering (Chapter 5), and also through the inclusion of reinforcements (Chapter 7). Therefore, one method of increasing the material mechanical properties may be to increase the amount of  $\beta$ -resin present in the system. However, increasing  $\beta$ -resin content may also increase the mass loss from the system, which results in increased material porosity. Thus additional studies are required to find optimum MCMB compositions.

The conclusion was made that *initial sample density* is an important parameter which governs the properties of the final material. Therefore, methods of producing green samples with higher green relative density should be investigated. This may be possible through the use of alternative processes, such as hot isostatic pressing (HIP). Further, it may be possible to reduce or *eliminate the swelling* event observed at lower temperatures ( $< 600$  K), e.g. by optimized calcination process. Specifically, an external force applied to the sample during heat treatment may physically restrain the sample from swelling. This may lead to greater values of shrinkage and better bonding between particles.

As indicated in Chapters 6 and 7, one of the major problems with forming composite systems with MCMB is the reduced relative green density that results when

reinforcement phases are introduced. The effect of porosity was discussed in Chapter 2, and although the sintering of reinforcement phases was observed (Chapter 6), it is likely that eliminating porosity by this method will be slow. Thus, *polymeric decomposition*, as discussed in Chapter 6, is a potential method for introducing reinforcements while maintaining high initial density. Additional work to test the effect of this process on mechanical properties is warranted. Further, there may be other polymeric precursors which contain other elements, such as Ti, W, B, Fe, etc., that could also be used to form nanosized reinforcements in-situ. The results reported in Chapter 7 show that, at the same level of porosity, composite systems have superior mechanical properties over pure MCMB.



## REFERENCES

- Aggarwal RK, Bhatia G, Bahl OP, Punjabi N. Effect of calcination conditions of self-sintering mesocarbon microbeads on the characteristics of resulting graphite. *Journal of materials science* 2000; 35:5437-5442.
- Bhatia G, Aggarwal RK, Punjabi N, Bahl OP. Effect of sintering temperature on the characteristics of carbons based on mesocarbon microbeads. *Journal of materials science* 1997; 32:135-139.
- Brooks JD, Taylor GH. The formation of graphitizing carbons from the liquid phase. *Carbon* 1965;3:185.
- Callister WD. *Materials science and engineering (an introduction)*. New York, NY: Wiley; 1997.
- Collings PJ, Hird M. *Introduction to liquid crystals – chemistry and physics*. London: Taylor & Francis; 1997.
- Czosnek C, Janik J, Olejniczak Z. Silicon carbide modified carbon materials. Formation of nanocrystalline SiC from thermochemical processes in the system coal tar pitch/poly(carbosilane). *Journal of cluster science* 2002; 13:487-502.
- Dillon F, Murdie N, Parker C, Pigford J, Wood M, Hayes D, Hemsted S. Sintered mesocarbon microbeads as a friction material. AlliedSignal invention disclosure, 1998.
- Fischbach DB. The kinetics and mechanism of graphitization. *Chemistry and physics of carbon* 1971; 7: 1-105.
- Fitzer E, Manocha LM. *Carbon reinforcements and carbon / carbon composites*. Berlin: Springer; 1998.
- Franklin RE. Crystallite growth in graphitization and non-graphitizing carbons. *Proceedings of the royal society* 1951; A209: 196-218.
- Gao Y, Song H, Chen X. Preparation of C/C composite using mesocarbon microbeads as matrix. *Journal of materials science letters* 2002; 21(13):1043-1045.

Gao Y, Song H, Chen X. Self-sinterability of mesocarbon microbeads (MCMB) for preparation of high-density isotropic carbon. *Journal of materials science* 2003, 38: 2209-2213.

Garcia-Rosales C, Ordas N, Oyarzabal E, Echeberria J, Balden M, Lindig S, Behrisch R. Improvement of the thermo-mechanical properties of fine grain graphite by doping with different carbides. *Journal of nuclear materials* 2002; 307-311: 1282-1288.

German RM. *Liquid phase sintering*. New York, NY: Plenum Press; 1985.

German RM. *Sintering theory and practice*. New York, NY: Wiley; 1996.

Green DW, ed. *Perry's chemical engineers' handbook*. New York, NY: McGraw-Hill; 1997.

Hoffmann WR, Hüttinger KJ. Demonstration of spontaneous liquid-phase sintering of mesophase powders. *Carbon* 1993; 31:259-262.

Hoffmann WR, Hüttinger KJ. Sintering of powders of polyaromatic mesophase to high-strength isotropic carbons – I. Influence of the raw material and sintering conditions on the properties of the carbon materials. *Carbon* 1994; 32: 1087-1103.

Hu XB, Zhong S, Zhao BY, Hu KA. Processing of an aqueous tape casting of mesocarbon microbeads for high-performance carbonaceous lamination. *Carbon* 2003; 41, 2285-2293.

Hu XB, Zhao BY, Hu KA. Thermal behaviors of mesocarbon microbeads and physical properties of carbon plates. *Journal of materials science* 2004; 39:1735-1741.

Iwashita N, Park CR, Fujimoto H, Shiraishi M, Inagaki M. Specification for a standard procedure of x-ray diffraction measurements on carbon materials. *Carbon* 2004; 42:701-714.

Lachter J, Bragg RH, Close E. Graphical analysis of processes with multiple activation energies. *Journal of applied physics* 1986; 60:1941-1843.

Li J, Hausner H. Reactive wetting in the liquid-silicon/solid-carbon system. *Journal of the American ceramics society* 1996; 79:873-80.

Marsh H, Menendez R. In: *Introduction to carbon science*. H. Marsh, ed. London: Butterworth; 1989.

Marsh H, Rodriguez-Reinoso F, eds. *Sciences of carbon materials*. Publicaciones de la Universidad de Alicante, 2000.

Martinez-Escandell M, Carreira P, Rodriguez-Valero MA, Rodriguez-Reinoso F. Self-sintering of carbon mesophase powders: effect of extraction/washing with solvents. *Carbon* 1999; 37:1662-1665.

McEnaney B. Structure and bonding in carbon materials. In: Burchell TD, ed. *Carbon Materials for Advanced Technologies*. New York, NY: Pergamon; 1999.

Mirhabibi A, Rand B, Banghshahi S, Aga Baba Zadeh R. Graphite flake carbon composites with a 'sinterable' microbead matrix. I. Mechanical properties. *Carbon* 2003; 41: 1593-1603.

Moriyama R, Kumagai H, Hayashi J, Yamaguchi C, Mondori J, Matsui H, Chiba T. Formation of mesophase spheres from a coal tar pitch upon heating and subsequent cooling observed by an in situ H-NMR. *Carbon* 2000; 38: 749.

Nagayama K, Torii T, Hatano H, Fukuda N. A sintering mechanism of KMFC green compact for high density carbon blocks. *Kawasaki Steel Technical Report* 1993; 28:5-10

Ozaki JI, Nishiyama Y. The changes in the structure and some physical properties of mesocarbon microbeads by heat treatment. *Carbon* 1987; 25:697-701.

Pacault A. The kinetics of graphitization. *Chemistry and physics of carbon* 1971; 7:107-155.

Perez-Maqueda LA, Criado JM, Real C. Kinetics of the initial stage of sintering from shrinkage data: simultaneous determination of activation energy and kinetic model from a single nonisothermal experiment. *Journal of the American ceramics society* 2002; 85 (4): 763-768.

Pigeon RG, Varma A, Miller AE. Some factors influencing the formation of reaction-bonded silicon nitride. *Journal of materials science* 1993; 28:1919-36.

Rahaman MN. *Ceramic processing and sintering*. New York, NY: Marcel Dekker; 1995.

Richerson DW. *Modern ceramic engineering: Properties, processing, and use in design*. 2<sup>nd</sup> ed. New York, NY: Marcel Dekker; 1992.

Romanoski GR, Burchell TD. Fracture in graphite. In: Burchell TD, ed. *Carbon Materials for Advanced Technologies*. New York, NY: Pergamon; 1999.

Varner JR. Fracture modes and appearances in ceramics. In: *ASM Handbook, Volume 11: Failure analysis and prevention*, eds. Becker WT, Shipley RJ. 1991.

Wang YG, Egashira M, Ishida S, Korai Y, Mochida I. Microstructure of mesocarbon microbeads prepared from synthetic isotropic naphthalene pitch in the presence of carbon black. *Carbon* 1999; 37:307-314.

Wang YG, Chang YC, Ishida S, Korai Y, Mochida I. Stabilization and carbonization properties of mesocarbon microbeads (MCMB) prepared from a synthetic naphthalene isotropic pitch. *Carbon* 1999; 37:969-976.

Wang YG, Korai Y, Mochida I. Carbon disc of high density and strength prepared from synthetic pitch-derived mesocarbon microbeads. *Carbon* 1999; 37:1049-1057.

Whittemore OJ, Varela JA. Pore distributions and pore growth during the initial stages of sintering. In: Kuczynski GC, editor. *Sintering Processes, Materials Science Research*, vol 13, New York; Plenum: 1980; 51-60.

Xiaohao C, Shenghua L, Yuansheng J, Huaihe S. A study of tribological performance and tribo-induced graphitization of meso-carbon microbeads. *Tribology Letters* 2003; 14, 53-59.